Characteristics of Robust Mesoscale Eddies in the Gulf of Mexico

Yingli Zhu[1] and Xinfeng Liang[1]

[1]University of Delaware

November 23, 2022

Abstract

Although several studies on mesoscale eddies in the Gulf of Mexico (GoM) have been conducted, a comprehensive study on their temporal and spatial characteristics is still lacking. In this study, we combine three eddy detection algorithms to detect eddies from the 26-year sea surface height record in the GoM and examine their characteristics. We find that many eddy characteristics in the GoM are associated with the Loop Current (LC). For the seasonal variability, in the eastern GoM, more cyclonic eddies (CEs) in the eastern part of the LC appear in spring, likely related to a larger gradient of background density, and more CEs and anticyclonic eddies (AEs) in the western part of the LC occur in fall, in line with a weakened LC. However, eddies in the western GoM show a more apparent biannual variability, which is mostly related to wind seasonality. For the low-frequency variability, eddy occurrence in the eastern part of the LC is related to the extent of northward penetration of the LC, while in the western part of the LC is related to the LC strength. In addition, the northward penetration of the LC can affect the eddy amplitude. In the western GoM, the low-frequency variability of eddy occurrence is related to the surface circulation strength. This study can serve as an up-to-date reference for eddy-related investigations in the GoM.

Characteristics of Robust Mesoscale Eddies in the Gulf of Mexico

Yingli Zhu*, Xinfeng Liang

School of Marine Science and Policy, University of Delaware, Lewes, DE 19958

* Corresponding to: yzhu@udel.edu

To be submitted to JGR-Oceans

Key Points:

- Eddies in the eastern Gulf of Mexico are related to the Loop Current, particularly its density, northward penetration and strength.
- Eddies in the western Gulf of Mexico exhibit biannual and low-frequency variabilities, which are likely related to wind variability.
- Increasing trends and climate-mode related variations of eddies are detected, although they are not significant in the present record.

Abstract

Although several studies on mesoscale eddies in the Gulf of Mexico (GoM) have been conducted, a comprehensive study on their temporal and spatial characteristics is still lacking. In this study, we combine three eddy detection algorithms to detect eddies from the 26-year sea surface height record in the GoM and examine their characteristics. We find that many eddy characteristics in the GoM are associated with the Loop Current (LC). For the seasonal variability, in the eastern GoM, more cyclonic eddies (CEs) in the eastern part of the LC appear in spring, likely related to a larger gradient of background density, and more CEs and anticyclonic eddies (AEs) in the western part of the LC occur in fall, in line with a weakened LC. However, eddies in the western GoM show a more apparent biannual variability, which is mostly related to wind seasonality. For the low-frequency variability, eddy occurrence in the eastern part of the LC is related to the extent of northward penetration of the LC, while in the western part of the LC is related to the LC strength. In addition, the northward penetration of the LC can affect the eddy amplitude. In the western GoM, the low-frequency variability of eddy occurrence is related to the surface circulation strength. This study can serve as an up-to-date reference for eddy-related investigations in the GoM.

Plain Language Summary

Mesoscale eddies play an important role in transporting ocean properties and materials, as well as in affecting the development of hurricanes in the Gulf of Mexico (GoM). In this study, characteristics of mesoscale eddy in the GoM including how they vary with space and time are examined using sea surface height data. We find that many eddy characteristics are closely related to the Loop Current (LC), the dominant circulation feature in the GoM. Eddy number varies with season and could be related to the seasonal variability of density structure and strength of the LC. However, eddies in the western GoM show a more apparent biannual variability, resulting from the influence of winds. Moreover, the interannual to decadal variability of eddy number is in the eastern GoM associated with the northward movement and the strength of the LC, and in the western GoM associated with the circulation strength related to wind forcing. The eddy characteristics reported in this study are useful for understanding phenomena affected by mesoscale eddies, such as the variability of ocean heat and the development of hurricanes in the GoM.

Keywords: Gulf of Mexico, Loop Current, mesoscale eddies, eddy characteristics, winds

1 Introduction

Mesoscale eddies are ubiquitous in the Gulf of Mexico (GoM). Different types of eddy have been identified, such as the Loop Current Eddy (LCE), the Loop Current Frontal Eddy (LCFE), and eddies that are not directly related to the Loop Current (LC). Those eddies are crucial in transporting heat, salt/freshwater, and other materials in the GoM (e.g., Beron-Vera et al., 2018; Brokaw et al., 2019; Chang & Oey, 2010; Meunier et al., 2018). Besides, those eddies can modify the atmospheric environment. In particular, hurricanes in the GoM can be intensified when encountering warm-core rings by absorbing a large amount of heat from eddies (e.g., Bosart et al., 2000; Hong et al., 2000).

Various measurements, including drifters, gliders, mooring, and satellite data, have been used to characterize eddies in the GoM (e.g., Elliott, 1982; Hamilton, 1992; Hamilton et al., 1999; Kirwan et al., 1984; Lewis et al., 1989; Meunier et al., 2018; Paluszkiewicz et al., 1983; Rivas et al., 2008; Rudnick et al., 2015; Vukovich & Maul, 1985; Zhang et al., 2019). Some eddy characteristics, such as diameter and propagation speed, have been reported in previous studies. For instance, LCEs have a diameter of 200 to 400 km, a surface swirling speed exceeding 0.5 m s^{-1}, and an average propagating speed of 2 to 5 km day^{-1} (e.g., Elliott, 1982; Kirwan et al., 1984; Kirwan et al., 1988; Vukovich & Crissman, 1986). The LCE path occupies a broad band in the center of the basin with a mean west-southwest track (Hamilton et al., 1999). Different from LCEs, mesoscale cyclonic eddies (CEs) have a relatively small diameter of 80 to 150 km (Hamilton, 1992; Jouanno et al., 2016; Le Hénaff et al., 2014; Vukovich & Maul, 1985; Vukovich, 2007). In addition, large CEs with a 200 km diameter have been observed in the central GoM when the LC is retracted to the south (Le Hénaff et al., 2014).

Statistical and comprehensive analyses of eddies over the whole GoM using in situ data and satellite infrared or ocean color data are difficult (e.g., Vukovich, 2007). In situ data cannot give continuous monitoring over the whole GoM. The nearly uniform sea surface temperature (SST) in summer and the extensive cloud cover hinder us from discerning eddies from the satellite infrared or ocean color maps (e.g., Sturges & Leben, 2000; Vukovich & Maul, 1985). In contrast, altimeter observed sea surface height (SSH) data are available in all weather conditions and are the most complete source of detecting mesoscale eddies. Although some temporal and spatial distributions of eddy characteristics have been obtained from the absolute dynamic topography (ADT) maps or along-track SSH anomalies, they are based on short-period altimeter data with record lengths of 2 to 4 years (Brokaw et al., 2020; Leben & Born, 1993) or are focused on one specific type of eddy, such as the LCFE (Le Hénaff et al., 2014). Eddy characteristics in the GoM, such as propagation, seasonal, and low-frequency (interannual to decadal) variability, are not clear. Nowadays, with the satellite observed SSH data that span more than 26 years, we can conduct a more comprehensive analysis of the characteristics of mesoscale eddies in the GoM.

To detect and describe eddies, a variety of automatic eddy detection and tracking algorithms have been developed. Chelton et al. (2007) use a physical parameter, Okubo-Weiss (OW) parameter (Okubo, 1970; Weiss, 1991) to detect mesoscale eddies. Geometric properties, such as the closed SSH or streamline contours, have also been used to define eddy domains (e.g., Chaigneau et al., 2008; Chelton et al., 2011; Faghmous et al., 2015; Le Vu et al., 2018). Moreover, hybrid methods that combine the physical parameters and geometric properties have been proposed to discern mesoscale eddies (Halo et al., 2014; Kang & Curchitser, 2013). Different eddy detection algorithms have their advantages and drawbacks. For example, the OW method is sensitive to the noise in the SSH data, and the approaches that use geometrical properties are sensitive to the interval searching for closed contours (Le Vu et al., 2018; Lian et al., 2019). There is no best algorithm because the eddy definition is elastic among different studies (Kurian et al., 2011).

In this study, to find eddies that are less sensitive to the eddy detection algorithms, a method that combines three previously used eddy detection algorithms is developed and applied to the 26-year SSH maps in the GoM. Robust characteristics of eddies in the GoM can be derived by examining the eddies detected with the new method. The paper is organized as follows: data and details of the eddy detection and tracking algorithms are presented in section 2. Characteristics of the detected eddies, including basic eddy characteristics, eddy trajectories, seasonal and low-frequency variabilities of eddies are reported in section 4. Conclusions and discussions are given in section 5.

2 Data and Processing

2.1 Data

Gridded ADT data from multi-mission altimeter satellites provided by the Copernicus Marine Environment Monitoring Service (CMEMS) were used for eddy detection. The ADT data span from 1 January 1993 to 13 May 2019 with a daily time interval. ADT data rather than sea level anomalies (SLAs) were selected because artificial eddies could be identified in SLAs (e.g., Laxenaire et al., 2018). Although the spatial resolution of the ADT provided is 0.25 degrees, its effective spatial resolution is controlled by many factors, such as the along-track smoothing and the spatial correlation scale (Pujol et al., 2016).

To examine the effective spatial resolution of the gridded ADT product in the GoM, TOPEX/Poseidon (T/P) along-track ADT data from 2 January 1996 to 3 December 1999 were compared with the gridded ADT data (Figure 1). Gridded ADT data were first linearly interpolated to the ground tracks shown in Figure 1a. The wavenumber spectrum of the along-track and interpolated ADT data along one sample T/P track were then calculated and averaged over the selected T/P period (Figure 1b). Compared to the along-track ADT, the spectrum of the gridded ADT decreases by 50% at the wavelength of 200 km, which represents the effective spatial resolution of the gridded ADT data in the GoM. This finding is consistent with the spatial correlation scales used in the gridded product processing (Pujol et al., 2016) and corresponds to an e-folding scale of about 37 km for an individual eddy (Chelton et al., 2011). Therefore, the gridded ADT product in the GoM can only resolve eddies with a radius larger than 37 km, and eddies with a radius smaller than 37 km are not considered in this study.

ADT data were further processed before they were used to detect eddies. First, since altimetry observations near the coast are less reliable (Castelao & He, 2013; Saraceno et al., 2008), ADT data at grid points that are 30 km or less away from the coast were discarded. Second, to make eddy features stand out from the large-scale background SSH field, a two-dimensional spatial filter with a cut-off wavelength of 1000 km was applied to the gridded ADT data. Eddy detection and tracking algorithms were then applied to the high-passed ADT fields.

Other variables were also explored to explain some of the detected eddy characteristics. The global atlas of the first-mode Rossby radius of deformation (Chelton et al., 1998) was used to calculate the standard first-mode Rossby wave propagation velocity, $c = -\beta R^2$, where β is the meridional variation of the Coriolis parameter and R is the first-mode Rossby radius of deformation. Since winds may play an important role in controlling the circulation and eddy activity in the GoM, wind stress and Ekman pumping velocity were derived from the gridded surface wind of the CCMP (Cross-Calibrated Multi-Platform) Version 2.0 (Atlas et al., 2011).

The daily wind product with a spatial resolution of 0.25 degrees was produced by RSS (Remote Sensing Systems). Word Ocean Atlas 2018 (WOA18) provides monthly climatologies of temperature (Locarnini et al., 2018) and salinity (Zweng et al., 2018) with a spatial resolution of 0.25 degrees. They were used to calculate the water density in the GoM. Moreover, the multivariate El Niño-Southern Oscillation (ENSO) index (MEI V2) (Zhang et al., 2019), North Atlantic Oscillation (NAO) index (Hurrell, 1995), and Atlantic Meridional Mode (AMM) index (Chiang & Vimont, 2004) were used to find the possible relationship between the eddy activity in the GoM and climate modes.

2.2 Eddy detection and tracking algorithms

An approach that combines three eddy detection algorithms proposed by Faghmous et al. (2015), Le Vu et al. (2018), and Halo et al. (2014) was developed to detect robust mesoscale eddies in the GoM. The three algorithms represent different approaches of automatic eddy detection and hereafter are referred to as F15, L18, and H14, respectively. In the F15 algorithm, eddies are defined as features of closed-contour SSH with one extremum. The H14 algorithm combines the OW parameter and geometrical properties of SSH. It identifies eddy as contained within a close loop of SSH and dominated by vorticity with the negative OW parameter. The L18 algorithm is a hybrid method based on physical parameters and geometrical properties of the velocity field. The eddy is contained within closed streamlines around an eddy center with a local maximum normalized angular momentum.

Due to the limited resolution of the gridded ADT field, a minimum of 9 pixels was used in the F15 algorithm and a minimum eddy radius of 37 km was used in the other two algorithms. Also, a minimum eddy amplitude of 2 cm was applied due to the accuracy of the SSH product (Pujol et al., 2016). The three eddy detection algorithms were implemented to the high-passed ADT field, yielding daily mesoscale eddies. An example of the detected eddies on 10 January 1993, as marked by the black circles in Figures 2a-2c, shows that some eddy can be detected by one algorithm but cannot be detected by the others. The three algorithms, F15, L18, and H14, gave rise to a total of 165123, 156347, and 131980 eddies in the GoM over the examined period, respectively.

We focus on the mesoscale eddies that can be detected by all three algorithms and define them as the robust eddies in the GoM. First, common pixels occupied by the eddies from all the three algorithms were found. Eddies from the H14 algorithm were used as basis eddies. For each eddy, if the number of common eddy pixels exceeded 50% of that from the H14 algorithm, the eddy was considered robust and kept for further processing. An example of robust eddies on 10 January 1993 is shown in Figure 2d. Since anticyclones detected in the area occupied by the LC may represent the core part of the LC, anticyclones with their southern boundary south of 23.5°N and with their eddy center within the rectangular marked in Figure 2d were discarded. The rectangular was chosen based on the climatology position of the LC (Vukovich, 2007).

The resulting robust eddies were then tracked with an algorithm developed by Penven et al. (2005), which was also used in Halo et al. (2014). An eddy in one frame is treated as the same eddy in the subsequent frame if the non-dimensional parameter between the two eddies with the same polarity, $D = \sqrt{(\Delta X/X_0)^2 + (\Delta R/R_0)^2 + (\Delta \xi/\xi_0)^2 + (\Delta Z/Z_0)^2 + (\Delta A/A_0)^2}$, is minimum, where ΔX is the spatial distance between the eddy centers, ΔR is the variation of eddy radius, $\Delta\xi$ is the variation of vorticity, ΔZ is the variation of mean SSH, ΔA is the variation of amplitude, X_0 is the typical length scale of 80 km, R_0 is the typical radius of 80 km, ξ_0 is the typical vorticity of 10^{-5} s^{-1}, Z_0 is the typical variation of mean SSH of 0.1 m, and A_0 is the typical variation of amplitude of 0.1 m. Eddy merging and splitting due to eddy-eddy interactions or other factors are not considered in this tracking algorithm. Because the temporal correlation scales of gridded ADT data are about 30 days at latitudes of the GoM (Pujol et al., 2016), only eddies with a lifetime greater than 30 days are examined in this study.

3 Results

3.1 Basic Eddy Characteristics

Distributions of some basic eddy characteristics are presented in Figure 3. Apparent differences between anticyclonic eddies (AEs) and CEs appear in their amplitude, eddy scale, and eddy intensity (Figures 3a-3c). The distribution of eddy amplitude is more skewed toward smaller values for AEs than CEs. Nevertheless, there are more large-amplitude (>0.25 m) AEs than CEs in the GoM. In contrast, the distribution of the eddy scale, defined as the radius with the maximum rotational speed (Chelton et al., 2011), is more skewed toward larger values for AEs than for CEs. These results are generally consistent with a recent study (Brokaw et al., 2020). Following Mason et al. (2019), we used the ratio of amplitude to radius to measure the intensity of eddies and found more CEs than AEs with an intensity larger than 1 mm/km.

The distributions of the maximum rotational speed, advective nonlinearity, and eddy lifetime are similar for AEs and CEs (Figures 3d-3f). More than 35% of eddies have a maximum rotational speed larger than 0.5 m s^{-1} so that eddies in the GoM can be highly nonlinear. The nonlinearity of eddy is then assessed with the advective nonlinearity parameter, U/C, where U is the maximum rotational speed and C is the translation speed of eddy. Eddies with $\mathrm{U/C} > 1$ can advect trapped fluid within the eddy interior when they translate (Chelton et al., 2011). Almost all the detected eddies have $\mathrm{U/C} > 1$, confirming that eddies in the GoM are highly nonlinear. Moreover, nearly 23% of AEs have a lifetime longer than 100 days but only 9% of CEs can live longer than 100 days, which is consistent with previous conclusions that CEs are small and short-lived compared to LCEs (Rudnick et al., 2015).

To illustrate their spatial distributions, some eddy characteristics were mapped into regular grids and shown in Figure 4. We first examined the properties of AEs (Figures 4a-4c and 4g-4i). Since AEs within the climatology LC are not considered in this study, no AE characteristics are seen in the LC region. AEs occur frequently in the northwestern GoM, are more likely generated in the northwestern tip of the LC, and are mostly dissipated in the northwestern GoM and north of the LC (Figures 4a-4c). Median values of the AE amplitude, scale, and rotational speed are large northwest of the LC, which is likely related to the large-scale LCEs shed from the LC (Figures 4g-4i). In contrast to AEs, CEs occur most frequently at the LC neck, in the northwestern and the southwestern GoM (Figure 4d). More CEs are generated in the eastern part of the LC, at the LC neck, and in the southwestern GoM, and are prone to dissipate at the LC neck and along the western boundary of the GoM (Figures 4e-4f). In addition, CEs have the largest amplitude and rotational speed at the LC neck and in the eastern part of the LC. The scale of CEs shows relatively large values at the LC neck and in the southwestern GoM (Figures 4j-4l).

3.2 Eddy Propagation

Trajectories of eddies generated in the eastern (east of 90°W) and western (west of 90°W) GoM were examined separately (Figures 5a-5b). AEs and CEs generated in the eastern GoM can travel into the western GoM (Figure 5a). Some AEs, mainly the LCEs, can arrive at the western boundary. In contrast, CEs that cross the 90°W longitude can only travel limited distances in the western GoM and CEs generated around the Campeche Bank do not travel or lose tracks along the western part of the LC. These are consistent with the previous conclusion that LCFE motions along the northern and eastern LC are decoupled from the LCFE motions along the southwestern

LC (Walker et al., 2009). In the eastern part of the LC, CEs mainly travel along the southward flowing LC. Eddies generated in the western GoM do not affect the eastern GoM (Figure 5b).

We also tracked back the eddies that are dissipated in the eastern and western GoM (Figures 5c-5d). Eddies dissipated in the eastern GoM mainly origin in the eastern GoM (Figure 5c). In contrast, some of the eddies dissipated in the western GoM originate from the eastern GoM (Figure 5d). Trajectories of AEs from the east to the southwest are in a broad meridional band, consistent with the broad paths of LCEs revealed in previous studies (e.g., Hamilton et al., 1999; Vukovich & Crissman, 1986; Vukovich, 2007).

Eddy propagation velocities were estimated by least-squares fitting the positions of eddy centers as a function of time in overlapping 30-day segments of each eddy's trajectory. Figure 6 shows the mean eddy propagation speeds and directions. Mean eddy propagating speed is highly variable in the GoM and ranges from 0.03 to 6 km day^{-1}. In particular, large values are found in the eastern part of the LC and the southwestern GoM. In the peripheral of the LC, the large speed and eddy propagation direction are related to the advection of the LC. In the western GoM, the dominant eddy propagation direction is to the west.

The eddy speed in the western GoM has a similar magnitude as the first-mode Rossby wave propagation speed (Figure 6b), which is close to that with small background mean currents (Chelton et al., 2011). For instance, the spatial average of the zonal eddy speed in the marked region (square in Figure 6) is 2.7 km day^{-1} and is close to the average value of the first-mode Rossby wave propagation speed (~2.8 km day^{-1}). However, it should be noted that eddy speeds larger than the first-mode Rossby wave propagation speeds by 1 km day^{-1} were also found, which might be related to the background circulation.

3.3 Monthly Climatology of Eddies

Monthly climatology of eddy number varies geographically. First, monthly climatology of eddy number in the eastern and western parts of the LC was obtained, respectively (Figure 7). In the eastern part of the LC (region EL marked in Figure 5c), the number of AEs (CEs) is smallest in July (December) but is highest in December (June) (Figures 7a-7b), indicating an opposite phase between the seasonal variability of the AE and CE number. Development of mesoscale eddies in the eastern GoM has been shown to be related to baroclinic instability (e.g., Yang et al., 2020) that is associated with the horizontal gradient of background density. To explore the linkage between the eddy number and the background density gradient, the monthly climatology of density gradient averaged in the eastern part of the LC and the upper 1000 m is presented along with the eddy number in Figures 7a-7b. The density gradient is large from March to August with more mean available potential energy that could be transferred to eddy energy.

The seasonal variability of the AE number does not follow that of the density gradient (Figure 7a). Figure 5c shows that most AEs in the eastern part of the LC are locally generated and dissipated in the northeastern corner of the GoM where the LC can barely reach. More AEs are observed in winter when the LC is relatively weak or is less penetrative (not shown) and factors such as winds may play more roles in the northeastern GoM. In contrast to AEs, the seasonal variability of the CE number more likely follows that of the mean density gradient in the eastern part of the LC (Figure 7b). Given that CEs in the eastern part of the LC are mainly LCFEs, the seasonal variability of the CE number can be related to the density structure that is largely controlled by the LC.

In the western part of the LC (region WL marked in Figure 5c), AEs, which are mainly composed of LCEs, are most frequent in October (Figure 7c). The shedding time of LCEs has been shown to be related to the seasonal winds in the GoM and the Caribbean Sea (Chang & Oey, 2012) and fluctuations from the Caribbean Sea (Chang & Oey, 2012, 2013; Murphy et al., 1999; Oey et al., 2003). The seasonal LC strength defined as the surface current speed averaged over one region close to the Yucatan Channel (Figure 5d) is shown along with the AE number (Figure 7c). The AE number peaks with the weakest LC in October. Chang & Oey (2013) have shown that eddy shedding tends to occur shortly after the minimum Yucatan vorticity and velocity. It should be noted that the LC strength could not be related to the minor peak of AE number from March to May when other factors such as winds may play a more important role (Chang & Oey, 2012). In addition, the seasonal variability of the CE number is presented with the LC strength in Figure 7d and is also in the opposite phase with that of the LC strength. Strong LC in spring and summer corresponds to fewer CEs, and weak LC in fall and winter corresponds to more CEs. The generation of CEs near the western edge of the Loop Current has been related to the LCE shedding (Zavala-Hidalgo et al., 2003). As a result, more CEs are likely observed with a weakened LC that could be accompanied by LCE shedding (Chang & Oey, 2013).

In the western GoM, the seasonal variability of eddy number in three regions, R1, R2, and R3 (Figure 5c), shows regional variability (Figure 8). In the northwestern GoM (region R1) more AEs occur in spring and summer, but in the southwestern GoM (region R3) more AEs are found in summer and winter (Figures 8a and 8e). In the central-western GoM (region R2), the least AEs and CEs are observed in July and April, respectively (Figures 8c-8d). The seasonal variability of CE number is nearly in opposite phase with that of AE number in the northwestern and southwestern GoM (Figures 8a-8b and 8e-8f). Overall, AEs and CEs in the western GoM indicate a biannual variability.

Eddy activities are closely related to the background circulation and winds (e.g., Chen et al., 2011). Large downwelling induced by the wind stress curl in the GoM results in a strong anticyclonic circulation. To examine the role of winds, the monthly climatology of Ekman pumping velocity was also calculated in the three regions. Generally, strong downwelling corresponds to more AEs, while weak downwelling or strong upwelling corresponds to more CEs (Figure 8). On exception is for AEs in the central-western GoM. One possible reason is that LCEs travel into the central-western GoM to complicate the AE seasonality (Figure 5a).

Despite partial contributions from the LCEs, the seasonal circulation in the western GoM largely results from the seasonal winds (DiMarco et al., 2005; Molinari, 1978; Morey et al., 2005; Nowlin Jr. et al., 2005; Sturges et al., 1993; Vázquez De La Cerda et al., 2005). For example, Figure 9 shows Ekman pumping, wind stress, and surface current climatology in two seasons, summer and fall. The stronger northwestward winds in the western GoM during summer (Figure 9a) induce stronger downwelling in the deep western GoM and stronger upwelling along the western coast, which generate an enhanced anticyclonic circulation (Figure 9c). The enhanced downwelling is favorable for developing AEs (e.g., Chi et al., 1998; Mkhinini et al., 2014). AEs can be observed along the boundary of the anticyclonic circulation in the western GoM, while CEs are less observed especially south of 25°N where the anticyclonic circulation dominates (Figure 9c). The relatively weak westward winds in fall in the western GoM (Figure 9b) generate weak downwelling in the central-western GoM and weak upwelling in the deep southwestern GoM, inducing cyclonic circulation in the semi-enclosed Bay of Campeche (e.g., DiMarco et al., 2005) (Figure 9d). The enhanced upwelling is favorable for developing CEs (e.g., Chi et al., 1998). Consequently, more CEs are observed in the southwest and fewer AEs are observed.

In addition to the seasonality observed in the eddy number, the seasonal variability of eddy amplitude was examined. The monthly climatology of median eddy amplitude in five regions marked in Figure 5c is presented in Figures 10 and 11. Since eddy amplitude is not normally distributed, median eddy amplitude was used to mitigate the potential influence of amplitude outliers. We suspected that the LC variability might influence the magnitude of the eddies in the eastern GoM, especially on the LCEs. The northern boundary of the LC that is defined as the northernmost position of the ADT contour at 500 mm is shown with the monthly climatology of eddy amplitude in the eastern GoM (Figure 10). AEs in the western part of the LC that are mainly LCEs have the largest seasonality with large amplitude in summer when the LC can extend further to the north (Figure 10c). However, the monthly climatology of CE amplitude along the LC and AE amplitude in the eastern part of the LC does not agree well with that of the northern boundary of the LC (Figures 10a-8b and 8d), implying other factors exist in determining the eddy amplitude.

The monthly climatology of AE amplitude in the western GoM (Figures 11a, 11c, and 11e) is noisier than that of AE number (Figure 8). Since wind forcing is important in the western GoM, the monthly climatology of Ekman pumping velocity induced by the wind stress curl is also presented in Figure 11. Monthly climatology of AE amplitude is less likely related to winds. CEs in the northwestern (Region 1) and central-western GoM (Region R2) have large amplitude from August to October when weak downwelling is observed (Figures 11b and 11d). Nevertheless, CE amplitude in the southwestern GoM (Region 3) has a poor correspondence to the wind climatology (Figure 11f). Compared to the seasonal variability of eddy number that is closely related to winds, the seasonal variability of eddy amplitude is less apparent and is merely related to winds over specific times and regions such as in the northwestern GoM.

3.4 Low-frequency Variability of Eddies

The climate variability in the GoM has been related to remote climate forcing such as ENSO and NAO (e.g., Rodriguez-Vera et al., 2019). The eddy activity in the GoM could be affected by various climate modes, such as ENSO (e.g., Philander, 1990), NAO (e.g., Wallace & Gutzler, 1981), and AMM (e.g., Chiang & Vimont, 2004), To test that, a linear regression model that includes a linear trend, MEI, NAO index, and AMM index was applied to the monthly AE and CE number in the eastern and western GoM. Eddy numbers and the climate indices were smoothed with the one-year moving average before the regression to remove high-frequency variabilities.

An increasing number of LCEs over 2001-2010 has been found in previous studies (Lindo-Atichati et al., 2013; Vukovich, 2012). Nevertheless, no long-term variability of AEs and CEs in the eastern and western GoM has been reported. In the eastern GoM, the linear trends of the AE and CE number per month from 1993 to 2018 are -0.02 ± 0.7 (±1σ) $year^{-1}$ and 0.51 ± 0.45 (±1σ) $year^{-1}$, respectively. In the western GoM, the linear trends of AE and CE number per month are 0.48 ± 0.49 (±1σ) $year^{-1}$ and 0.86 ± 0.59 (±1σ) $year^{-1}$, respectively. An increasing eddy number is observed, but the linear trends are not statistically significant at the 5% significance level.

Regression coefficients of the three climate indices are not significant as well. For AEs in the eastern GoM, the coefficient of determination of AMM is 0.14 and is larger than that of other predictors. AE number in the eastern GoM might be related to the climate variability in the tropical Atlantic represented by AMM. CE number in the eastern GoM and AE number in the western GoM cannot be explained by the three climate modes. For CEs in the western GoM, the coefficient of determination of NAO is 0.15 that is the largest among the three climate indices. CE number in the western GoM might be related to the climate variability in the North Atlantic represented by NAO. However, the regression coefficients are not statistically significant and only a small portion of eddy number variance can be explained by the three climate modes, indicating that the role of the remote climate variability in changing the eddy activity in the GoM is small or cannot be detected from the linear model.

To obtain the dominant mode of the low-frequency (interannual to decadal) variability of eddies, empirical orthogonal function (EOF) analysis was applied to the annual sums of AE and CE number, respectively (Figure 12). The first EOF mode of AE and CE occurrence explains 75% of the variance. The spatial pattern of the first EOF mode shows that the major low-frequency variability of AE occurrence is in the central-western GoM (Figure 12a), while the major low-frequency variability of CE occurrence is in the northwestern GoM and along the LC (Figure 12b). Since the background current strength could be important in affecting the low-frequency eddy activity (Chen et al., 2011), mode-1 PCs of AE and CE number were compared with the surface current speed averaged in the western GoM (Figures 12c-12d) where the largest eddy number variability is found. Both mode-1 PCs of AE and CE number are correlated with the mean surface current speed in the western GoM, indicating that more eddies are accompanied by stronger background circulation in the western GoM. In the western GoM, the mean current strength is anticorrelated with the mean Ekman pumping velocity with a significant correlation of -0.78. The correlation between the mode-1 PC of AE and CE number and the mean current speed is 0.64 and 0.5, respectively. Although the correlation value of 0.5 is not significant at the 5% significance level, the low-frequency eddy activity is closely related to the strength of the circulation in the western GoM that is partly driven by winds. It should be noted that LCEs translating to the western GoM can modify the eddy activity in the western GoM (Figure 5a).

In the eastern GoM, the low-frequency variability of eddy number and possibly related factors, including the northern boundary of the LC and the LC strength in the eastern GoM, were examined (Figure 13). Similar to the seasonal variability, the interannual variability of the AE and CE number is different between the eastern and western sides of the LC. Figures 13a-13b show the interannual variations of the CE and AE number in the eastern part of the LC along with the northern boundary position of the LC. The CE number and the northern boundary position of the LC are correlated with a significant correlation of 0.67, indicating that the CE number in the eastern part of the LC increases with the northward penetration of the LC on the interannual to decadal time scale (Figure 13a). In contrast, the AE number is anticorrelated with the northern boundary position of the LC with an insignificant correlation of -0.52, indicating that more AEs in the eastern part of the LC may exist when the LC retracts to the south (Figure 13b).

In the western part of the LC, the low-frequency variability of eddies is distinct from that in the eastern part of the LC and no significant correlation is found between the eddy number and the northern boundary position of the LC. Similar to the seasonal variability of CEs, the interannual variability of CE number in the western part of the LC is anticorrelated with the LC strength with a significant correlation value of -0.56 (Figure 13c). However, the correlation between the interannual variability of AE number in the western part of the LC and the LC strength is 0.14. Previous studies have shown that perturbations coming from the Caribbean Sea (Huang et al., 2013) and the topography of the northern Campeche (Chérubin et al., 2006) also contribute to the eddy activity along the western edge of the LC.

Eddy amplitude in the GoM exhibits apparent low-frequency variability as well. EOF analysis was applied to the annual median values of AE and CE amplitude. Figure 3a shows that eddy amplitude is not normally distributed. To mitigate the potential influence of amplitude outliers, median eddy amplitude in each year was selected for the EOF analysis. The first EOF mode of AE and CE amplitude explains 89% and 94% of the variance, respectively. The spatial pattern of the first EOF mode shows that the major variability of AE amplitude is in the central GoM and associated with new separated LCEs (Figure 14a). The decadal variability of AE amplitude seems to vary with the northern boundary of the LC after 2000 (Figure 14c). The LC that intrudes more northward could have more water mass that can be included in LCEs. But other factors should be more important in determining the AE amplitude before 2000. Compared to the AE amplitude, CEs have a smaller amplitude variability. The major variability of CE amplitude is in the eastern part of the LC and is associated with LCFEs (Figure 14b). LCFE amplitude seems to be related to the extent of the LC penetration (Figure 14d). With a more northward penetration of the LC, CEs can have more time to intensify in the eastern part of the LC because of baroclinic instability (Donohue et al., 2016) and southward advection of positive potential vorticity anomalies induced by the topography (Le Hénaff et al., 2014; Le Hénaff et al., 2012).

4 Conclusions and Discussion

In this study, we presented characteristics of the robust mesoscale eddies in the GoM, including their spatial distributions, propagation features, seasonal and low-frequency variabilities. As expected, many eddy characteristics in the eastern GoM are closely related to the LC, which sheds large and strong LCEs and develops small-scale LCFEs (e.g., Brokaw et al., 2020; Le Hénaff et al., 2014). Among those eddies, only LCEs can travel a long distance from the eastern to the western GoM, as observed from other datasets (e.g., Vukovich 2007). Temporally mean propagation speeds are high in the eastern part of the LC and the southwestern GoM.

The temporal variability of eddy occurrence and amplitude, which is less reported in literature, shows manifest spatial patterns and dramatic differences between AEs and CEs. In the eastern GoM, more CEs in the eastern (western) part of the LC are observed in spring (fall), while more AEs in the eastern (western) part of the LC are observed in November-January (September-October). AEs have the strongest seasonality of amplitude in the western part of the LC with a large amplitude in summer. In the western GoM, more CEs in the northwestern and southwestern (central-western) GoM are found in spring and fall (fall), but more AEs in the northwest and southwestern (central-western) GoM occur in May-July (November-January). Seasonal variability of CE amplitude in the western GoM is also observed with large amplitude from August to October in the central and northwestern GoM, while the seasonal variability of AE amplitude is not apparent.

The seasonal and low-frequency variability of eddies in the eastern and western parts of the LC is related to different metrics of the LC variability. On the seasonal time scale, CE number in the eastern and western parts of the LC is likely associated with the mean density structure and the LC strength, respectively. AE number in the western part of the LC is also related to the LC strength. Different from the AE number, the AE amplitude in the western part of the LC is associated with the extent of the northward penetration of the LC. In the western GoM, winds play an important role in the seasonal variability of eddy occurrence but play a smaller role in the seasonal variability of eddy amplitude. On the interannual to the decadal time scale, CE number in the eastern and western parts of the LC is related to the extent of northward penetration of the LC and strength of the LC, respectively. In the western GoM, the surface circulation strength that is closely related to wind forcing is important for the low-frequency variability of eddy occurrence. In addition, the major low-frequency variability of AE and CE amplitude could be related to the extent of the LC northward penetration. It should be noted that the eddy activity in the western GoM could be complicated by LCEs traveling from the eastern GoM that changes the large-scale background circulation and generate companion eddies (e.g., Elliott, 1982; Meza-Padilla et al., 2019; Pérez-Brunius et al., 2013; Vidal et al., 1992; Romanou et al., 2004).

Since mesoscale eddies are important oceanic processes in the GoM for their roles in affecting both oceanic and atmospheric conditions, the reported eddy characteristics may provide insights in understanding phenomena affected by eddies. For example, the seasonal and low-frequency variabilities of eddies in different regions may induce both temporal and spatial variability of heat, salt/freshwater, and nutrients (e.g., Damien et al., 2018). The long-term change of eddy activity in the GoM can have significant influences on the future projection of ocean conditions. Although the linear trend of eddy occurrence is not significant in the current record, it indicates that climate change is likely changing the eddy activity in the GoM. Moreover, the eddy characteristics can affect the prediction of hurricanes that move across the GoM (e.g., Hong et al., 2000), so both weather and climate numerical models need to consider or reproduce these eddy characteristics for better predictions.

Note that eddy characteristics obtained in this study may include uncertainties caused by drawbacks in eddy detection and tracking algorithms despite a combination of three different eddy detection algorithms. For instance, geometrical properties in detection algorithms are sensitive to interval searching for closed contours (Lian et al., 2019). Besides, eddies may experience periods of eddy interaction, splitting, or merging, which is not considered in many tracking algorithms (e.g., Faghmous et al. 2015; Halo et al. 2014), including the one (Penven et al., 2005) used in this study. With the increasing knowledge of mesoscale eddies and improved eddy detection and tracking algorithms, more robust eddy characteristics will be obtained in future studies.

In this study, we focus on describing the characteristics of the robust mesoscale eddies in the GoM, and some characteristics such as the temporal and spatial patterns of eddies still need further dynamical explanations. In particular, the two sides of the LC show different seasonal and low-frequency variability that is associated with distinct LC metrics. Previous studies indicate that mesoscale eddies in the eastern GoM likely arise from dynamic instabilities, such as barotropic and baroclinic instabilities (e.g., Chérubin et al., 2006; Donohue et al., 2016; Pichevin & Nof, 1997; Sturges & Leben, 2000; Vukovich & Maul, 1985; Yang et al., 2020; Zavala-Hidalgo et al., 2003). In the future, dynamic analyses such as eddy energy diagnose may shed light on the detailed mechanisms of the temporal and spatial variability of mesoscale eddies in the GoM.

Acknowledgments

The work was supported in part by the Gulf of Mexico Research Initiative through Grant G-231804 and the National Aeronautics and Space Administration through Grant 80NSSC20K0757. SSH data used in this study is SEALEVEL_GLO_PHY_L4_REP_OBSERVATIONS_008_047 that was produced and provided by CMEMS (https://resources.marine.copernicus.eu/?option=com_csw&view=details&product_id=SEALEVEL_GLO_PHY_L4_REP_OBSERVATIONS_008_047). CCMP Version-2.0 vector wind analyses were produced by Remote Sensing Systems. Data are available at www.remss.com. The atlas of the first-baroclinic Rossby radius of deformation was downloaded at http://www-

po.coas.oregonstate.edu/research/po/research/rossby_radius/ (Chelton et al., 1998). The monthly climatologies of temperature and salinity were provided by WOA18 at https://www.nodc.noaa.gov/cgi-bin/OC5/woa18/woa18.pl (Atlas et al., 2011). The MEI, NAO index, and AMM index were downloaded at https://psl.noaa.gov/data/climateindices/list/.

References

Atlas, R., Hoffman, R. N., Ardizzone, J., Leidner, S. M., Jusem, J. C., Smith, D. K., & Gombos, D. (2011). A Cross-calibrated, Multiplatform Ocean Surface Wind Velocity Product for Meteorological and Oceanographic Applications. *Bulletin of the American Meteorological Society*, 92(2), 157-174. https://doi.org/10.1175/2010BAMS2946.1

Beron-Vera, F. J., Olascoaga, M. J., Wang, Y., Triñanes, J., & Pérez-Brunius, P. (2018). Enduring Lagrangian coherence of a Loop Current ring assessed using independent observations. *Scientific Reports*, 8(1), 11275. https://doi.org/10.1038/s41598-018-29582-5

Bosart, L. F., Bracken, W. E., Molinari, J., Velden, C. S., & Black, P. G. (2000). Environmental Influences on the Rapid Intensification of Hurricane Opal (1995) over the Gulf of Mexico. *Monthly Weather Review*, 128(2), 322-352. https://doi.org/10.1175/1520-0493(2000)128h0322:EIOTRIi2.0.CO;2

Brokaw, R. J., Subrahmanyam, B., & Morey, S. L. (2019). Loop current and eddy-driven salinity variability in the Gulf of Mexico. *Geophysical Research Letters*, 46(11), 5978-5986. https://doi.org/10.1029/2019GL082931

Brokaw, R. J., Subrahmanyam, B., Trott, C. B., & Chaigneau, A. (2020). Eddy surface characteristics and vertical structure in the Gulf of Mexico from satellite observations and model simulations. *Journal of Geophysical Research: Oceans*, 125(2), e2019JC015538. https://doi.org/10.1029/2019JC015538

Castelao, R. M., & He, R. (2013). Mesoscale eddies in the South Atlantic Bight. *Journal of Geophysical Research: Oceans*, 118(10), 5720-5731. https://doi.org/10.1002/ jgrc.20415

Chaigneau, A., Gizolme, A., & Grados, C. (2008). Mesoscale eddies off Peru in altimeter records: Identification algorithms and eddy spatio-temporal patterns. *Progress in Oceanography*, 79(2), 106-119. https://doi.org/10.1016/j.pocean.2008.10.013

Chang, Y.-L., & Oey, L.-Y. (2010). Eddy and Wind-Forced Heat Transports in the Gulf of Mexico. *Journal of Physical Oceanography*, 40(12), 2728-2742. https://doi.org/10.1175/2010JPO4474.1

Chang, Y.-L., & Oey, L.-Y. (2012). Why does the loop current tend to shed more eddies in summer and winter? *Geophysical Research Letters*, 39(5). https://doi.org/10.1029/2011GL050773

Chang, Y.-L., & Oey, L.-Y. (2013). Loop Current Growth and Eddy Shedding Using Models and Observations: Numerical Process Experiments and Satellite Altimetry Data. *Journal of Physical Oceanography*, 43(3), 669-689. https://doi.org/10.1175/JPO-D-12-0139.1

Chelton, D. B., deSzoeke, R. A., Schlax, M. G., El Naggar, K., & Siwertz, N. (1998). Geographical Variability of the First Baroclinic Rossby Radius of Deformation. *Journal of Physical Oceanography*, 28(3), 433-460. https://doi.org/10.1175/1520-0485(1998)028h0433:GVOTFBi2.0.CO;2

Chelton, D. B., Schlax, M. G., & Samelson, R. M. (2011). Global observations of nonlinear mesoscale eddies. *Progress in Oceanography*, 91(2), 167 - 216. https://doi.org/10.1016/j.pocean.2011.01.002

Chelton, D. B., Schlax, M. G., Samelson, R. M., & de Szoeke, R. A. (2007). Global observations of large oceanic eddies. *Geophysical Research Letters*, 34(15). https://doi.org/10.1029/2007GL030812

Chen, G., Hou Y., and Chu X. (2011). Mesoscale eddies in the South China Sea: Mean properties, spatiotemporal variability, and impact on thermohaline structure, *J. Geophys. Res.*, 116, C06018, https://doi.org/doi:10.1029/2010JC006716

Chérubin, L. M., Morel, Y., & Chassignet, E. P. (2006). Loop current ring shedding: The formation of cyclones and the effect of topography. *Journal of Physical Oceanography*, 36(4), 569-591. https://doi.org/10.1175/JPO2871.1

Chi, P.C., Chen, Y. & Lu, S. (1998). Wind-driven South China Sea deep basin warm-core/cool-core eddies. *J Oceanogr*. 54, 347–360. https://doi-org.udel.idm.oclc.org/10.1007/BF02742619

Chiang, J. C. H., & Vimont, D. J. (2004). Analogous Pacific and Atlantic Meridional Modes of Tropical Atmosphere–Ocean Variability, *Journal of Climate*, *17*(21), 4143-4158.

Damien, P., Pasqueron de Fommervault, O., Sheinbaum, J., Jouanno, J., Camacho-Ibar, V. F., & Duteil, O. (2018). Partitioning of the open waters of the Gulf of Mexico based on the seasonal and interannual variability of chlorophyll concentration. *Journal of Geophysical Research: Oceans*, 123, 2592-2614. https://doi.org/10.1002/2017JC013456

DiMarco, S.F., Nowlin, W.D., Jr. and Reid, R.O. (2005). A Statistical Description of the Velocity Fields from Upper Ocean Drifters in the Gulf of Mexico. In Circulation in the Gulf of Mexico: Observations and Models (eds W. Sturges and A. Lugo‐Fernandez). https://doi.org/10.1029/161GM08

Donohue, K., Watts, D., Hamilton, P., Leben, R., & Kennelly, M. (2016). Loop current eddy formation and baroclinic instability. Dynamics of Atmospheres and Oceans, 76, 195-216. (The Loop Current Dynamics Experiment) https://doi.org/10.1016/j.dynatmoce.2016.01.004

Elliott, B. A. (1982). Anticyclonic rings in the Gulf of Mexico. *Journal of Physical Oceanography*, 12(11), 1292-1309. https://doi.org/10.1175/1520-0485(1982)012h1292:ARITGOi2.0.CO;2

Faghmous, J. H., Frenger, I., Yao, Y., Warmka, R., Lindell, A., & Kumar, V. (2015). A daily global mesoscale ocean eddy dataset from satellite altimetry. *Scientific Data*, 2, 150028. https://doi.org/10.1038/sdata.2015.28

Halo, I., Backeberg, B., Penven, P., Ansorge, I., Reason, C., & Ullgren, J. (2014). Eddy properties in the Mozambique Channel: A comparison between observations and two numerical ocean circulation models. *Deep Sea Research Part II: Topical Studies in Oceanography*, 100, 38-53. https://doi.org/10.1016/j.dsr2.2013.10.015

Hamilton, P. (1992). Lower continental slope cyclonic eddies in the central Gulf of Mexico. *Journal of Geophysical Research: Oceans*, 97(C2), 2185-2200. https://doi.org/10.1029/91JC01496

Hamilton, P., Fargion, G. S., & Biggs, D. C. (1999). Loop Current Eddy Paths in the Western Gulf of Mexico. *Journal of Physical Oceanography*, 29(6), 1180- 1207. https://doi.org/10.1175/1520-0485(1999)029h1180:LCEPITi2.0.CO;2

Hong, X., Chang, S. W., Raman, S., Shay, L. K., & Hodur, R. (2000). The Interaction between Hurricane Opal (1995) and a Warm Core Ring in the Gulf of Mexico. *Monthly Weather Review*, 128(5), 1347-1365. https://doi.org/10.1175/1520-0493(2000)128h1347:TIBHOAi2.0.CO;2

Huang, H., Walker, N. D., Hsueh, Y., Chao, Y., & Leben, R. R. (2013). An Analysis of Loop Current Frontal Eddies in a 1/6° Atlantic Ocean Model Simulation. *Journal of Physical Oceanography*, 43(9), 1924-1939. https://doi.org/10.1175/JPO-D-12-0227 .1

Hurrell, J.W. (1995). Decadal trends in the North Atlantic Oscillation and relationships to regional temperature and precipitation. *Science*, 269, 676-679. https://doi.org/10.1126/science.269.5224.676

Jouanno, J., Ochoa, J., Pallàs-Sanz, E., Sheinbaum, J., Andrade-Canto, F., Candela, J., & Molines, J.-M. (2016). Loop Current Frontal Eddies: Formation along the Campeche Bank and Impact of Coastally Trapped Waves. *Journal of Physical Oceanography*, 46(11), 3339-3363. https://doi.org/10.1175/JPO-D-16-0052.1

Kang, D., & Curchitser, E. N. (2013). Gulf stream eddy characteristics in a high resolution ocean model. *Journal of Geophysical Research: Oceans*, 118(9), 4474-4487. https://doi.org/10.1002/jgrc.20318

Kirwan A. D., Lewis, J. K., Indest, A. W., Reinersman, P., & Quintero, I. (1988). Observed and simulated kinematic properties of loop current rings. *Journal of Geophysical Research: Oceans*, 93(C2), 1189-1198. https://doi.org/10.1029/JC093iC02p01189

Kirwan A. D., Merrell Jr., W. J., Lewis, J. K., & Whitaker, R. E. (1984). Lagrangian observations of an anticyclonic ring in the western gulf of mexico. *Journal of Geophysical Research: Oceans*, 89(C3), 3417-3424. https://doi.org/10.1029/JC089iC03p03417

Kurian, J., Colas, F., Capet, X., McWilliams, J. C., & Chelton, D. B. (2011). Eddy properties in the California Current System. *Journal of Geophysical Research: Oceans*, 116(C8). https://doi.org/10.1029/2010JC006895

Laxenaire, R., Speich, S., Blanke, B., Chaigneau, A., Pegliasco, C., & Stegner, A. (2018). Anticyclonic eddies connecting the western boundaries of Indian and Atlantic Oceans. *Journal of Geophysical Research: Oceans*, 123, 7651–7677. https://doi.org/10.1029/2018JC014270

Leben, R. R., & Born, G. H. (1993). Tracking loop current eddies with satellite altimetry. *Advances in Space Research*, 13(11), 325-333. https://doi.org/10.1016/0273-1177(93)90235-4

Le Hénaff, M., Kourafalou, V. H., Dussurget, R., & Lumpkin, R. (2014). Cyclonic activity in the eastern Gulf of Mexico: Characterization from along-track altimetry and in situ drifter trajectories. *Progress in Oceanography*, 120, 120-138. https://doi.org/10.1016/j.pocean.2013.08.002

Le Hénaff, M., Kourafalou, V. H., Morel, Y., & Srinivasan, A. (2012). Simulating the dynamics and intensification of cyclonic Loop Current Frontal Eddies in the Gulf of Mexico. *Journal of Geophysical Research: Oceans*, 117(C2). https://doi.org/10.1029/2011JC007279

Le Vu, B., Stegner, A., & Arsouze, T. (2018). Angular Momentum Eddy Detection and Tracking Algorithm (AMEDA) and Its Application to Coastal Eddy Formation. *Journal of Atmospheric and Oceanic Technology*, 35(4), 739-762. https://doi.org/10.1175/JTECH-D-17-0010.1

Lewis, J. K., Kirwan Jr., A. D., & Forristall, G. Z. (1989). Evolution of a warm-core ring in the Gulf of Mexico: Lagrangian observations. *Journal of Geophysical Research: Oceans*, 94(C6), 8163-8178. https://doi.org/10.1029/JC094iC06p08163

Lian, Z., Sun, B., Wei, Z., Wang, Y., & Wang, X. (2019). Comparison of Eight Detection Algorithms for the Quantification and Characterization of Mesoscale Eddies in the South China Sea. *Journal of Atmospheric and Oceanic Technology*, 36(7), 1361-1380. https://doi.org/10.1175/JTECH-D-18-0201.1

Lindo-Atichati, D., Bringas, F., & Goni, G. (2013). Loop current excursions and ring detachments during 1993-2009. *International Journal of Remote Sensing*, 34(14), 5042-5053. https://doi.org/10.1080/01431161.2013.787504

Locarnini, R. A., A. V. Mishonov, O. K. Baranova, T. P. Boyer, M. M. Zweng, H. E. Garcia, J. R. Reagan, D. Seidov, K. Weathers, C. R. Paver, and I. Smolyar, 2018. *World Ocean Atlas 2018, Volume 1: Temperature*. A. Mishonov Technical Ed.; NOAA Atlas NESDIS 81, 52 pp.

Mason, E., Ruiz, S., Bourdalle-Badie, R., Reffray, G., García-Sotillo, M., and Pascual, A. (2019) New insight into 3-D mesoscale eddy properties from CMEMS operational models in the western Mediterranean, *Ocean Science.*, 15, 1111–1131. https://doi.org/10.5194/os-15-1111-2019

Meunier, T., Pallás-Sanz, E., Tenreiro, M., Portela, E., Ochoa, J., Ruiz-Angulo, A., & Cusí, S. (2018). The vertical structure of a loop current eddy. *Journal of Geophysical Research: Oceans*, 123(9), 6070-6090. https://doi.org/10.1029/2018JC013801

Meza-Padilla, R., Enriquez, C., Liu, Y., & Appendini, C. M. (2019). Ocean circulation in the western Gulf of Mexico using self-organizing maps. *Journal of Geophysical Research: Oceans*, 124(6), 4152-4167. https://doi.org/10.1029/2018JC014377

Mkhinini, N., A. L. S. Coimbra, A. Stegner, T. Arsouze, I. Taupier-Letage, and K. Beranger (2014). Long-lived mesoscale eddies in the eastern Mediterranean Sea: Analysis of 20 years of AVISO geostrophic velocities, *Journal of Geophysical Research: Oceans*, 119, 8603–8626. https://doi.org/doi:10.1002/ 2014JC010176.

Molinari, R. L. (1978). The Relationship of the Curl of the Local Wind Stress to the Circulation of the Cayman Sea and the Gulf of Mexico. *Journal of Physical Oceanography*, 8(5), 779-784. https://doi.org/10.1175/1520-0485(1978)008h0779: TROTCOi2.0.CO;2

Morey, S. L., Zavala-Hidalgo, J., & O’Brien, J. J. (2005). The Seasonal Variability of Continental Shelf Circulation in the Northern and Western Gulf of Mexico from a High-

Resolution Numerical Model. In Circulation in the Gulf of Mexico: Observations and Models (eds W. Sturges and A. Lugo‐Fernandez). https://doi.org/10.1029/161GM16

Murphy, S. J., Hurlburt, H. E., & O'Brien, J. J. (1999). The connectivity of eddy variability in the Caribbean Sea, the Gulf of Mexico, and the Atlantic Ocean. *Journal of Geophysical Research: Oceans*, 104(C1), 1431-1453. https://doi.org/10.1029/1998JC900010

Nowlin, W.D., Jr., Jochens, A.E., DiMarco, S.F., Reid, R.O. and Howard, M.K. (2005). Low-Frequency Circulation Over the Texas-Louisiana Continental Shelf. In Circulation in the Gulf of Mexico: Observations and Models (eds W. Sturges and A. Lugo‐Fernandez). https://doi.org/10.1029/161GM17

Oey, L.-Y., Lee, H.-C., & Schmitz Jr., W. J. (2003). Effects of winds and Caribbean eddies on the frequency of loop current eddy shedding: A numerical model study. *Journal of Geophysical Research: Oceans*, 108(C10). https://doi.org/10.1029/2002JC001698

Okubo, A. (1970). Horizontal dispersion of floatable particles in the vicinity of velocity singularities such as convergences. *Deep Sea Research*, 17(3), 445 - 454. https://doi.org/10.1016/0011-7471(70)90059-8

Paluszkiewicz, T., Atkinson, L. P., Posmentier, E. S., & McClain, C. R. (1983). Observations of a loop current frontal eddy intrusion onto the West Florida Shelf. *Journal of Geophysical Research: Oceans*, 88(C14), 9639-9651. https://doi.org/10.1029/JC088iC14p09639

Philander SGH (1990). El Niño, La Niña, and the Southern Oscillation (Academic, London).

Penven, P., Echevin, V., Pasapera, J., Colas, F., & Tam, J. (2005). Average circulation, seasonal cycle, and mesoscale dynamics of the Peru current system: A modeling approach. *Journal of Geophysical Research: Oceans*, 110(C10). https://doi.org/10.1029/2005JC002945

Pichevin, T., & Nof, D. (1997). The momentum imbalance paradox. *Tellus A: Dynamic Meteorology and Oceanography*, 49(2), 298-319. https://doi.org/10.3402/tellusa.v49i2.14484

Pérez-Brunius, P., García-Carrillo, P., Dubranna, J., Sheinbaum, J., & Candela, J. (2013). Direct observations of the upper layer circulation in the southern gulf of mexico. *Deep Sea Research Part II: Topical Studies in Oceanography*, 85, 182-194. (Modern Physical Oceanography and Professor H.T. Rossby) https://doi.org/10.1016/j.dsr2.2012.07.020

Pujol, M.-I., Faugère, Y., Taburet, G., Dupuy, S., Pelloquin, C., Ablain, M., & Picot, N. (2016). DUACS DT2014: the new multi-mission altimeter data set reprocessed over 20 years. *Ocean Science*, 12(5), 1067–1090. https://doi.org/10.5194/os-12-1067-2016

Rivas, D., Badan, A., Sheinbaum, J., Ochoa, J., & Candela, J. (2008). Vertical Velocity and Vertical Heat Flux Observed within Loop Current Eddies in the Central Gulf of Mexico. *Journal of Physical Oceanography*, 38(11), 2461-2481. https://doi.org/10.1175/2008JPO3755.1

Rodriguez-Vera, G., R. Romero-Centeno, C. L. Castro, and V. M. Castro, (2019). Coupled Interannual Variability of Wind and Sea Surface Temperature in the Caribbean Sea and the Gulf of Mexico. *J. Climate*, **32**, 4263–4280, https://doi.org/10.1175/JCLI-D-18-0573.1.

Romanou, A., Chassignet, E. P., & Sturges, W. (2004). Gulf of Mexico circulation within a high-resolution numerical simulation of the North Atlantic Ocean. *Journal of Geophysical Research: Oceans*, 109(C1). https://doi.org/10.1029/2003JC001770

Rudnick, D. L., Gopalakrishnan, G., & Cornuelle, B. D. (2015). Cyclonic Eddies in the Gulf of Mexico: Observations by Underwater Gliders and Simulations by Numerical Model. *Journal of Physical Oceanography*, 45(1), 313-326. https://doi.org/10.1175/JPO-D-14-0138.1

Saraceno, M., Strub, P. T., & Kosro, P. M. (2008). Estimates of sea surface height and near-surface alongshore coastal currents from combinations of altimeters and tide gauges. *Journal of Geophysical Research: Oceans*, 113(C11). https://doi.org/10.1029/2008JC004756 Sturges, W., Evans, J. C., Welsh, S., & Holland, W. (1993). Separation of warm-core rings in the Gulf of Mexico. *Journal of Physical Oceanography*, 23(2), 250-268. https://doi.org/10.1175/1520-0485(1993)023h0250:SOWCRIi2.0.CO;2

Sturges, W. (1993), The annual cycle of the western boundary current in the Gulf of Mexico, *J. Geophys. Res.*, 98(C10), 18053-18068, https://doi.org/10.1029/93JC01730

Sturges, W., & Leben, R. (2000). Frequency of ring separations from the loop current in the Gulf of Mexico: A revised estimate. *Journal of Physical Oceanography*, 30(7), 1814-1819. https://doi.org/10.1175/1520-0485(2000)030h1814: FORSFTi2.0.CO;2

Vidal, V. M. V., Vidal, F. V., & Pérez-Molero, J. M. (1992). Collision of a loop current anticyclonic ring against the continental shelf slope of the western Gulf of Mexico. *Journal of Geophysical Research: Oceans*, 97(C2), 2155-2172. https://doi.org/10.1029/91JC00486

Vukovich, F. M. (2007). Climatology of ocean features in the Gulf of Mexico using satellite remote sensing data. *Journal of Physical Oceanography*, 37(3), 689-707. https://doi.org/10.1175/JPO2989.1

Vukovich, F. M. (2012). Changes in the loop current's eddy shedding in the period 20012010. International *Journal of Oceanography*, 2012, 18. https://doi.org/10.1155/ 2012/439042

Vukovich, F. M., & Crissman, B. W. (1986). Aspects of warm rings in the Gulf of Mexico. *Journal of Geophysical Research: Oceans*, 91(C2), 2645-2660. https://doi.org/10.1029/JC091iC02p02645

Vukovich, F. M., & Maul, G. A. (1985). Cyclonic Eddies in the Eastern Gulf of Mexico. *Journal of Physical Oceanography*, 15(1), 105-117. https://doi.org/10.1175/1520-0485(1985)015h0105:CEITEGi2.0.CO;2

Vázquez De La Cerda, A.M., Reid, R.O., DiMarco, S.F. and Jochens, A.E. (2005). Bay of Campeche Circulation: An Update. In Circulation in the Gulf of Mexico: Observations and Models (eds W. Sturges and A. Lugo‐Fernandez). https://doi.org/10.1029/161GM20

Wallace, J. M., & Gutzler, D. S. (1981). Teleconnections in the Geopotential Height Field during the Northern Hemisphere Winter, *Monthly Weather Review*, *109*(4), 784-812

Walker, N., Leben, R., Anderson, S., Feeney, J., Coholan, P., & Sharma, N. (2009). Loop current frontal eddies based on satellite remote sensing and drifter data (Tech. Rep. No. OCS Study MMS 2009-023). New Orleans, LA: U.S. Dept. of the Interior, Minerals Management Service, Gulf of Mexico OCS Region.

Weiss, J. (1991). The dynamics of enstrophy transfer in two-dimensional hydrodynamics. *Physica D: Nonlinear Phenomena*, 48(2), 273-294. https://doi.org/10.1016/0167-2789(91)90088-Q

Yang, Y., Weisberg, R. H., Liu, Y., & San Liang, X. (2020). Instabilities and Multiscale Interactions Underlying the Loop Current Eddy Shedding in the Gulf of Mexico. *Journal of Physical Oceanography*, 50(5), 1289-1317. https://doi.org/10.1175/JPO-D-19-0202.1

Zavala-Hidalgo, J., Morey, S. L., & O'Brien, J. J. (2003). Cyclonic Eddies Northeast of the Campeche Bank from Altimetry Data. *Journal of Physical Oceanography*, 33(3), 623-629. https://doi.org/10.1175/1520-0485(2003)033h0623:CENOTCi2.0.CO;2

Zhang, T, A. Hoell, J. Perlwitz, J. Eischeid, D. Murray, M. Hoerling and T. Hamill, 2019: Towards Probabilistic Multivariate ENSO Monitoring, *Geophys. Res. Lett.*, 46, DOI: 10.1029/2019GL083946

Zhang, Y., Hu, C., Liu, Y., Weisberg, R. H., & Kourafalou, V. H. (2019). Submesoscale and mesoscale eddies in the florida straits: Observations from satellite ocean color measurements. *Geophysical Research Letters*, 46(22), 13262-13270. https://doi.org/10.1029/2019GL083999

Zweng, M. M., J. R. Reagan, D. Seidov, T. P. Boyer, R. A. Locarnini, H. E. Garcia, A. V. Mishonov, O. K. Baranova, K. Weathers, C. R. Paver, and I. Smolyar, 2018. *World Ocean Atlas 2018, Volume 2: Salinity*. A. Mishonov Technical Ed.; NOAA Atlas NESDIS 82, 50 pp.

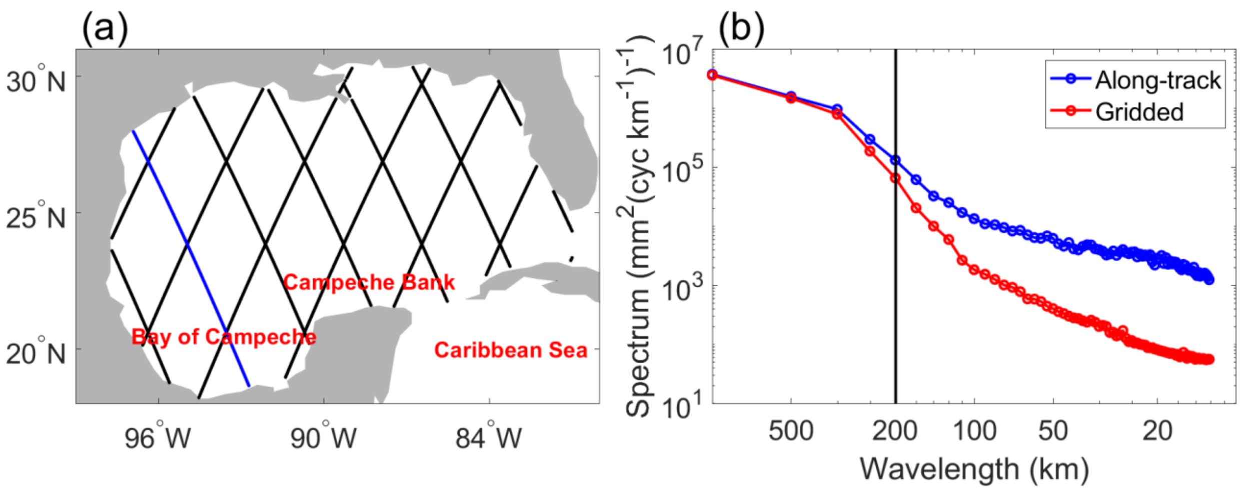

Figure 1. (a) Ground tracks of the T/P satellite in the GoM. The blue line represents the track along which the wavenumber spectrum of ADT was estimated. (b) Wavenumber spectrum of along-track and gridded ADT along the track marked in blue.

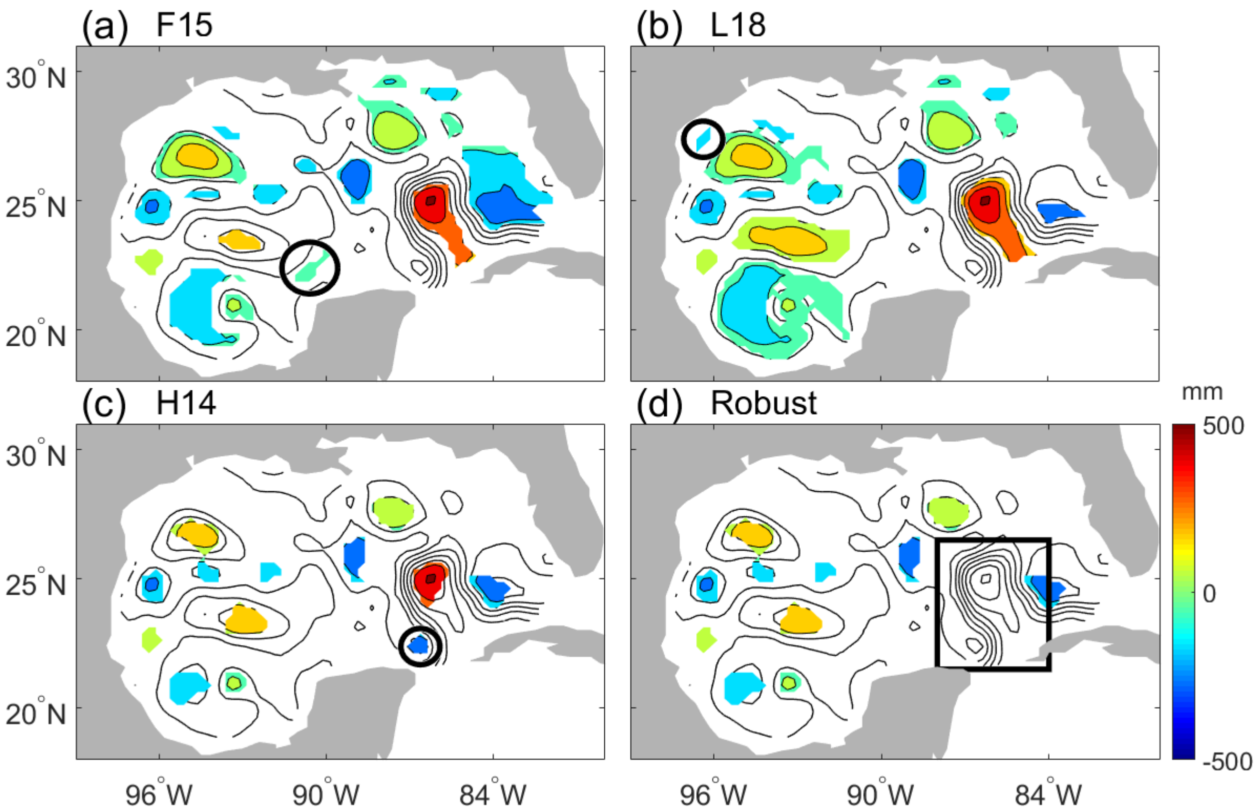

Figure 2. Snapshots of the high-passed ADT (contours) and detected eddies (shaded colors) on 10 January 1993. Eddies were detected by (a) F15 algorithm, (b) L18 algorithm, (c) H14 algorithm, and (d) robust detection algorithm. The black circle in (a), (b), and (c) encloses the eddy that was detected by one algorithm but not detected by the other two algorithms. The black rectangular denotes the LC region where anticyclones with the southern boundary south of 23.5°N were discarded.

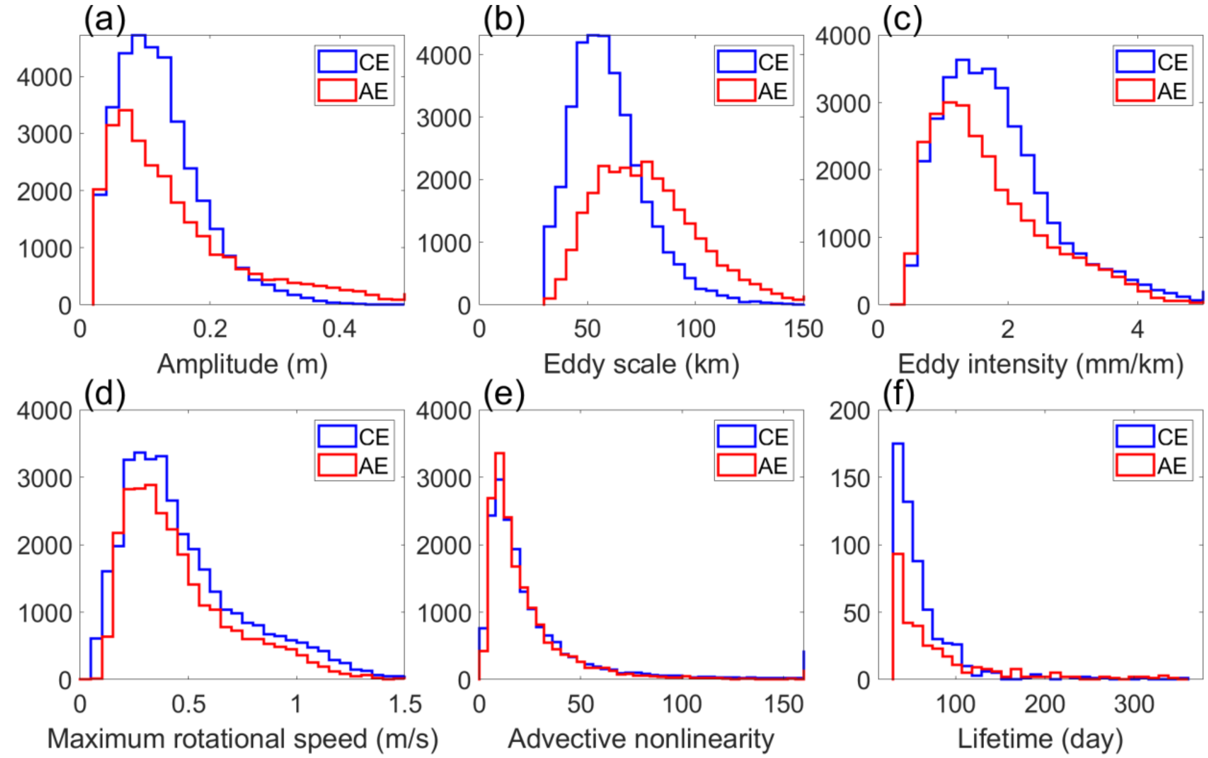

Figure 3. Histograms of basic eddy characteristics: (a) amplitude, (b) eddy scale, (c) eddy intensity, (d) maximum rotational speed, (e) advective nonlinearity, (f) lifetime.

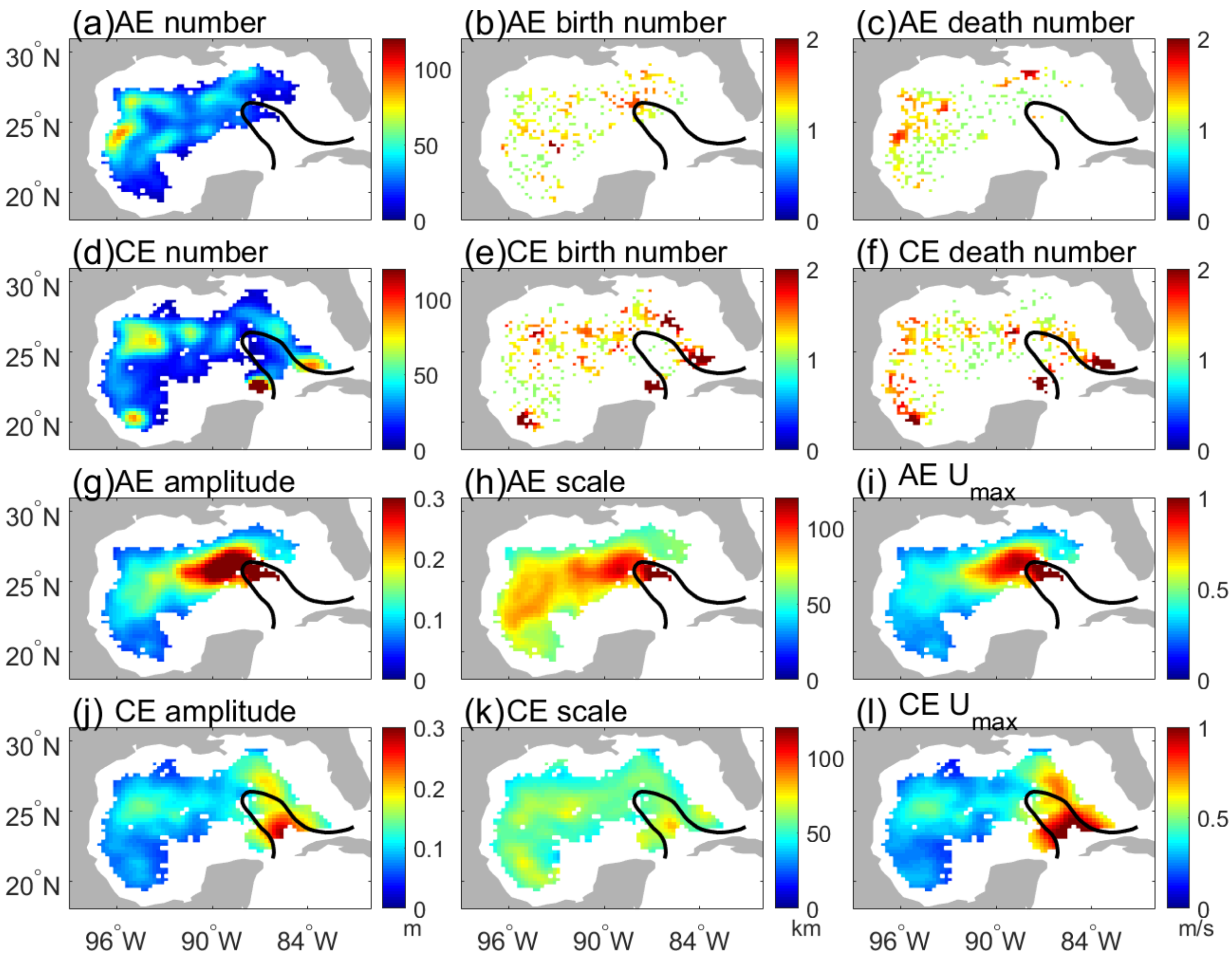

Figure 4. (a) AE number. (b) Number of newly generated AEs. (c) Number of terminated AEs. (d) CE number. (e) Number of new generated CEs. (f) Number of terminated CEs. (g) Median values of AE amplitude. (h) Median values of AE scale. (i) Median values of AE maximum rotational speed. (j) Median values of AE amplitude. (k) Median values of CE scale. (l) Median values of CE maximum rotational speed. The black line represents the mean ADT contour of 500 mm from 1993 to 2019. No AE characteristics are found within the LC because most AEs within the LC is not considered as shown in Figure 2d.

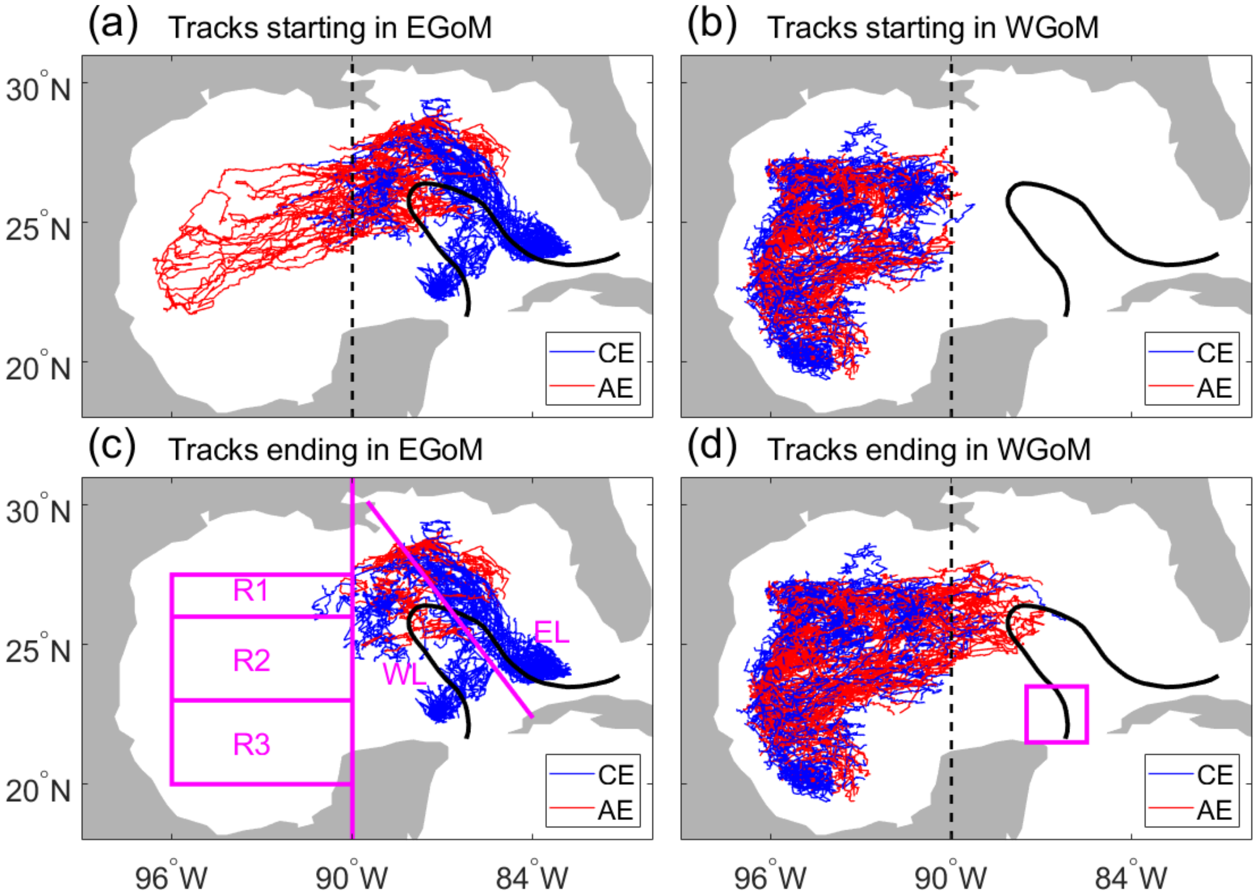

Figure 5. Trajectories of AEs (red lines) and CEs (blue lines) that are (a) generated in the eastern GoM, (b) generated in the western GoM, (c) dissipated in the eastern GoM, and (d) dissipated in the western GoM. The meridional line denotes the 90°W longitude separating the eastern and western GoM. The thick black line represents the mean ADT contour of 500 mm from 1993 to 2019. The three magenta rectangles in (c) represent three regions, R1, R2, and R3, where seasonal variability of eddies was examined in Figures 8 and 11. The tilted magenta line divides the western part (WL) and eastern part (EL) of the LC, where seasonal variability of eddies was examined in Figures 7 and 10. The magenta square in (d) marks the region over which the average surface current speed was calculated to represent the LC strength.

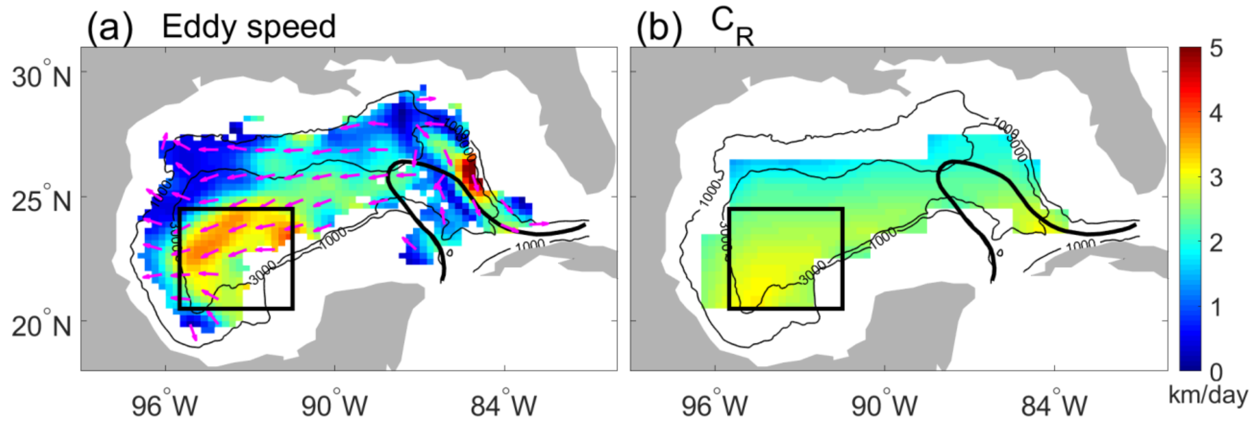

Figure 6. (a) Mean eddy propagation speeds (color map) and directions (magenta arrows). (b) First-mode Rossby wave propagation speeds. The black rectangular marks the relatively high-speed region. Thin black contours denote isobaths at 1000 and 3000 m. The thick black line represents the mean ADT contour of 500 mm from 1993 to 2019.

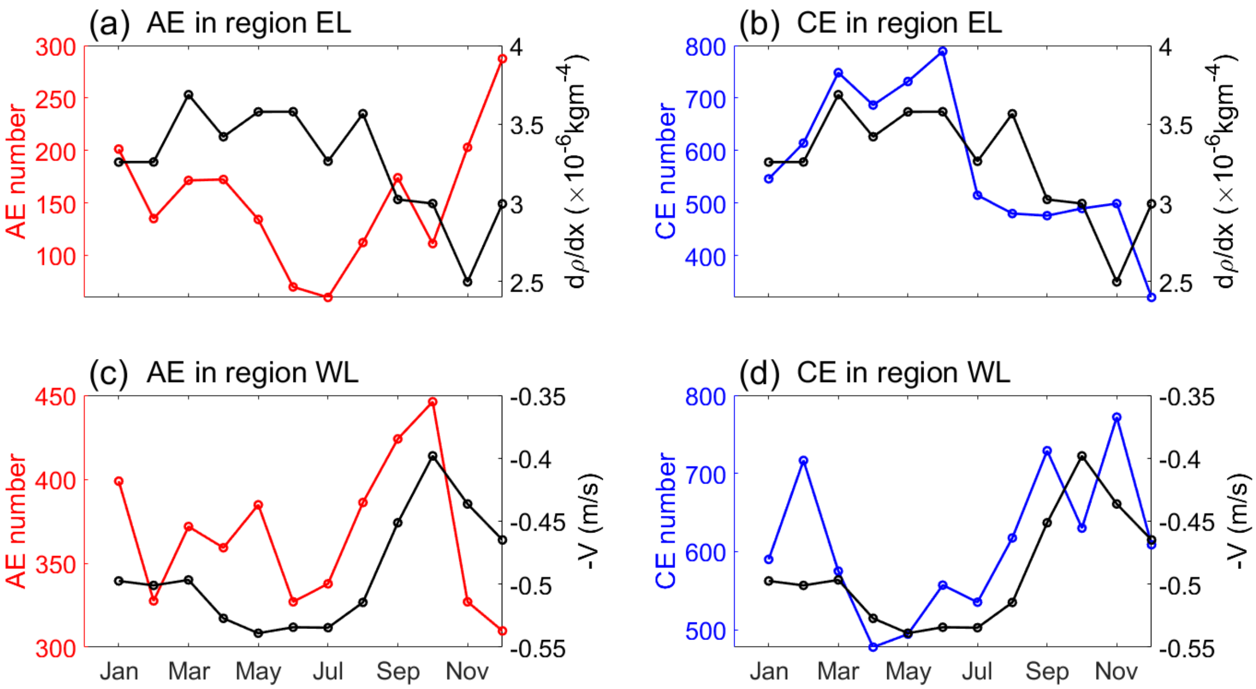

Figure 7. Monthly climatology of AE (red) and CE (blue) number in (a, b) the eastern part of the LC and in (c, d) the western part of the LC. The black line in (a) and (b) represents the monthly climatology of the density gradient averaged in the eastern part of the LC and the upper 1000 m, and the black line in (c) and (d) represents the minus surface current speed averaged in the region marked by the magenta square in Figure 5d. The Eastern part (EL) and the western part (WL) of the LC are marked in Figure 5c.

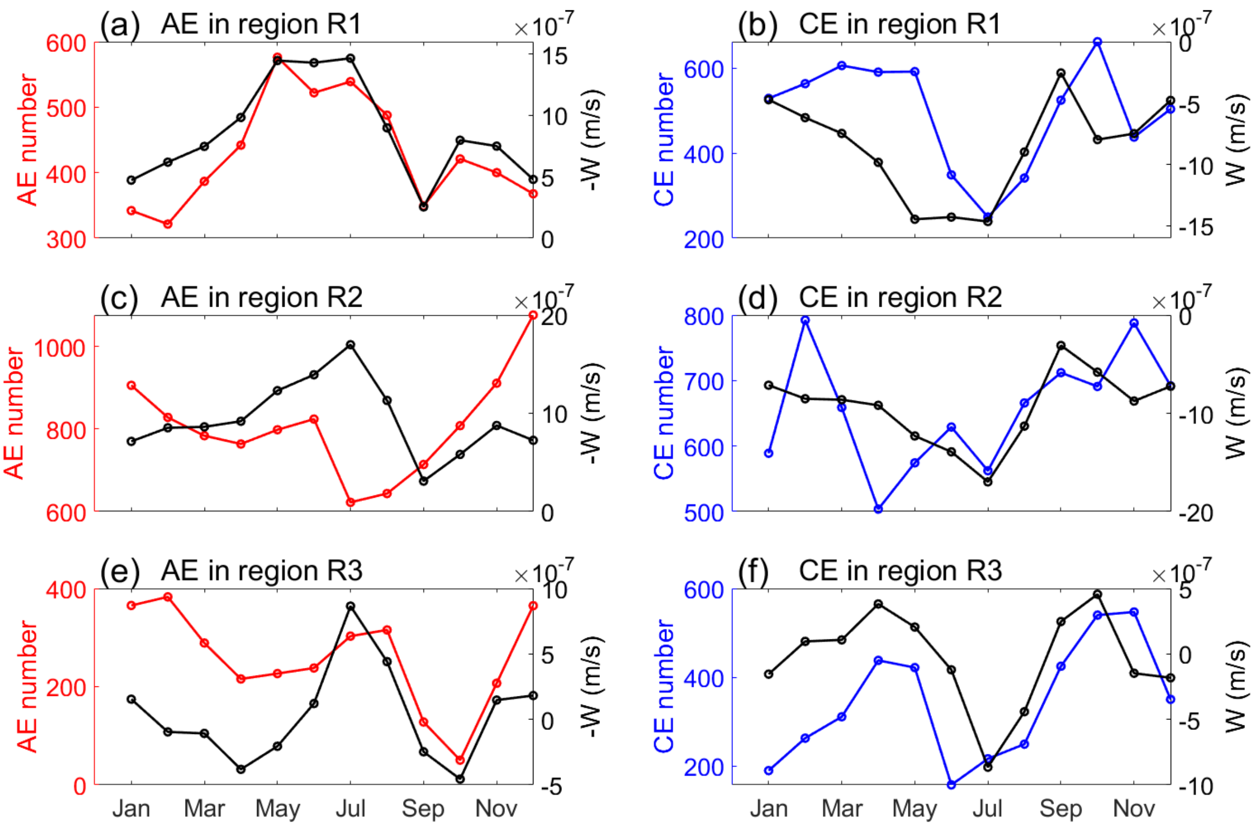

Figure 8. Monthly climatology of AE number (red) and CE number (blue) in (a, b) region R1, in (c, d) region R2, and in (e, f) region R3. The black line in (a), (c), and (e) represents the monthly climatology of the minus Ekman pumping velocity averaged in region R1, R2, and R3, respectively. The black line in (b), (d), and (f) represents the monthly climatology of the Ekman pumping velocity averaged in region R1, R2, and R3, respectively. Region R1, R2, and R3 are marked in Figure 5c.

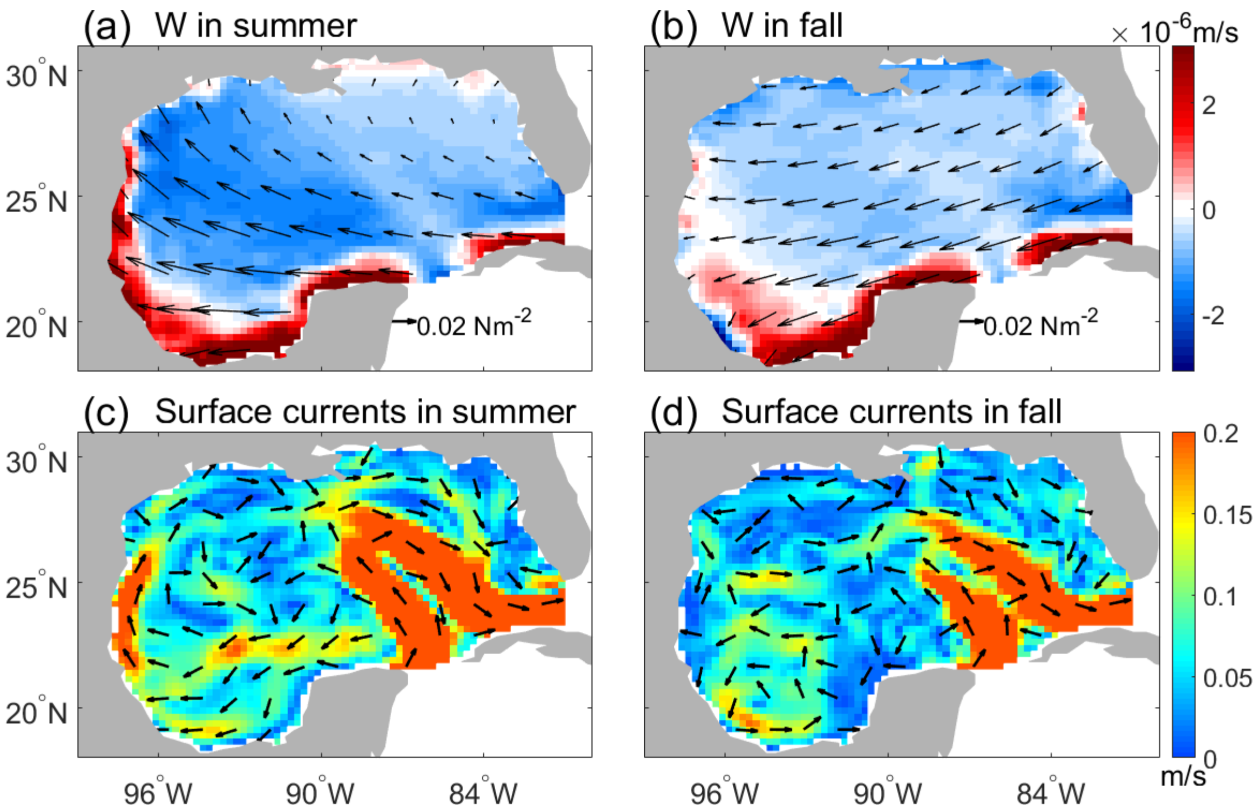

Figure 9. Climatology of Ekman pumping velocity (color map) and wind stress (black arrows) in summer (a), and in fall (b). Climatology of surface current speeds (color map) and current directions (black arrows) derived from ADT in summer (c), and in fall (d).

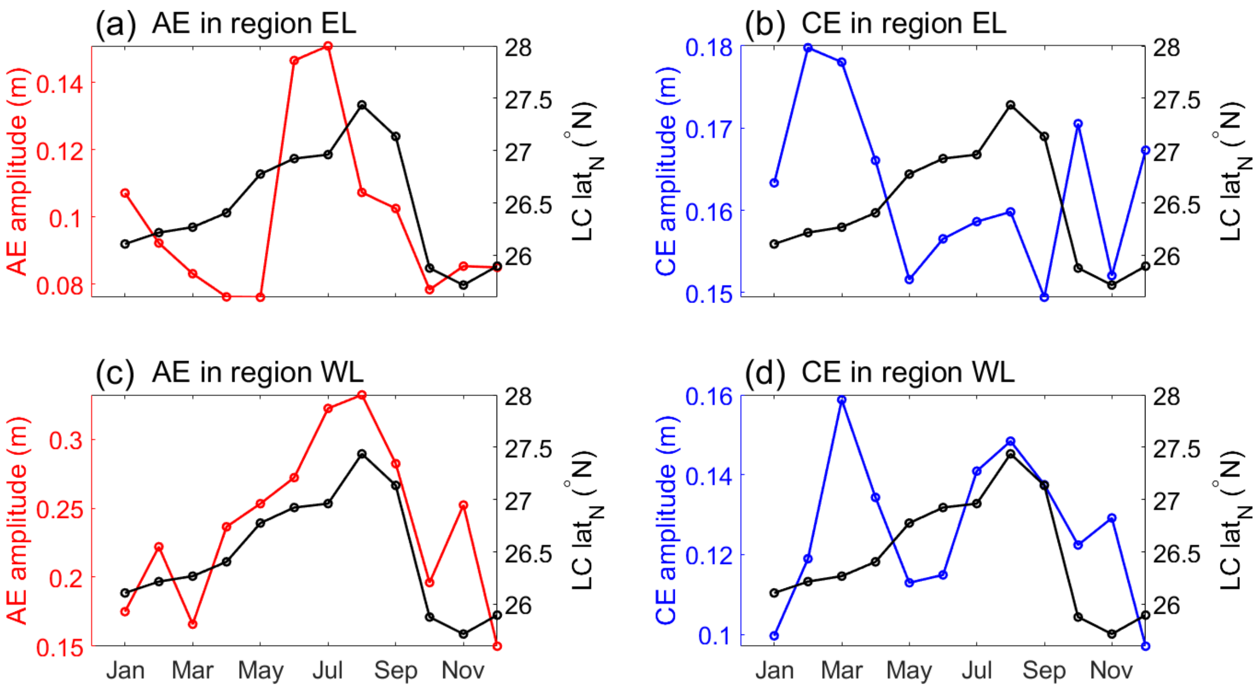

Figure 10. Monthly climatology of AE median amplitude (red) and CE median amplitude (blue) in (a, b) the eastern part of the LC and in (c, d) the western part of the LC. The black line represents the monthly climatology of the northern position of the LC. The Eastern part (EL) and the western part (WL) of the LC are marked in Figure 5c.

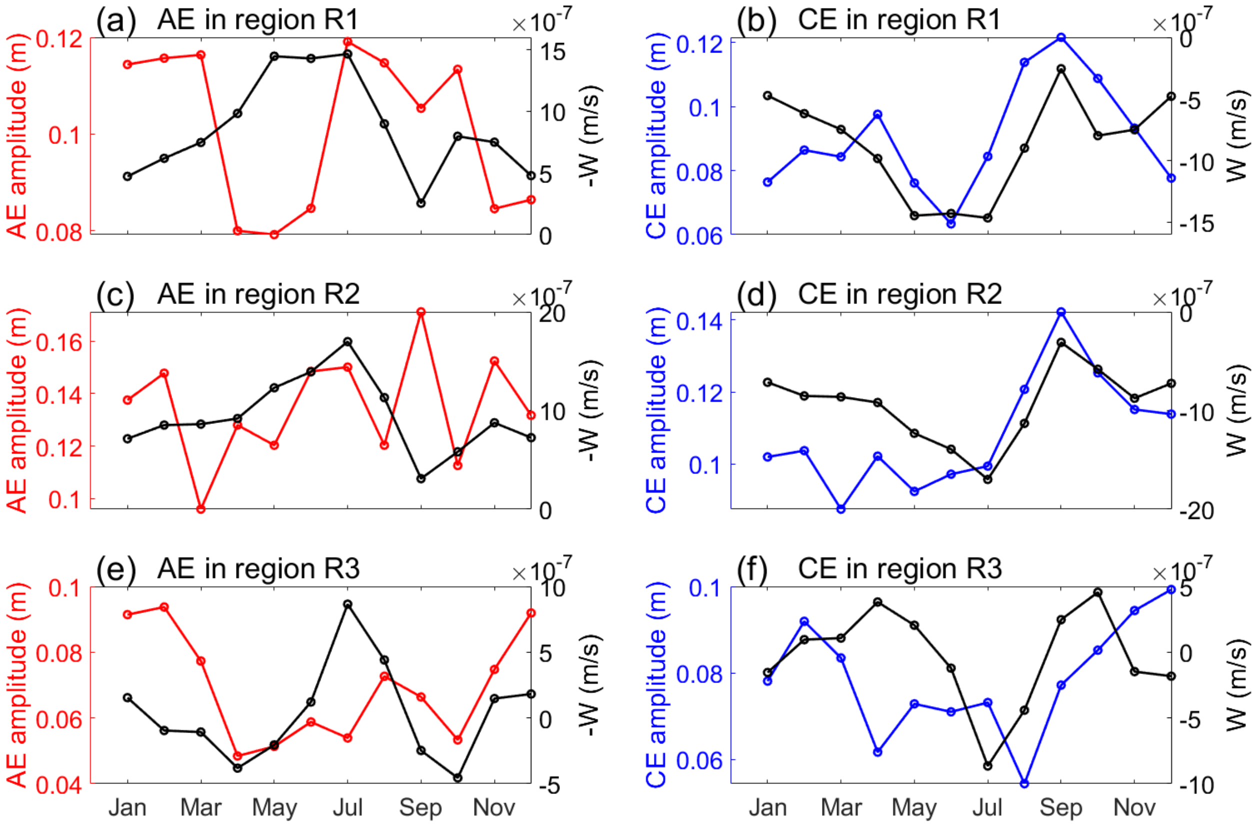

Figure 11. Monthly climatology of AE median amplitude (red) and CE median amplitude (blue) in (a, b) region R1, in (c, d) region R2, and in (e, f) region R3. The black line in (a), (c), and (e) represents the monthly climatology of the minus Ekman pumping velocity averaged in region R1, R2 andR3, respectively. The black line in (b), (d), and (f) represents the monthly climatology of the Ekman pumping velocity averaged in region R1, R2, and R3, respectively. Region R1, R2, and R3 are marked in Figure 5c.

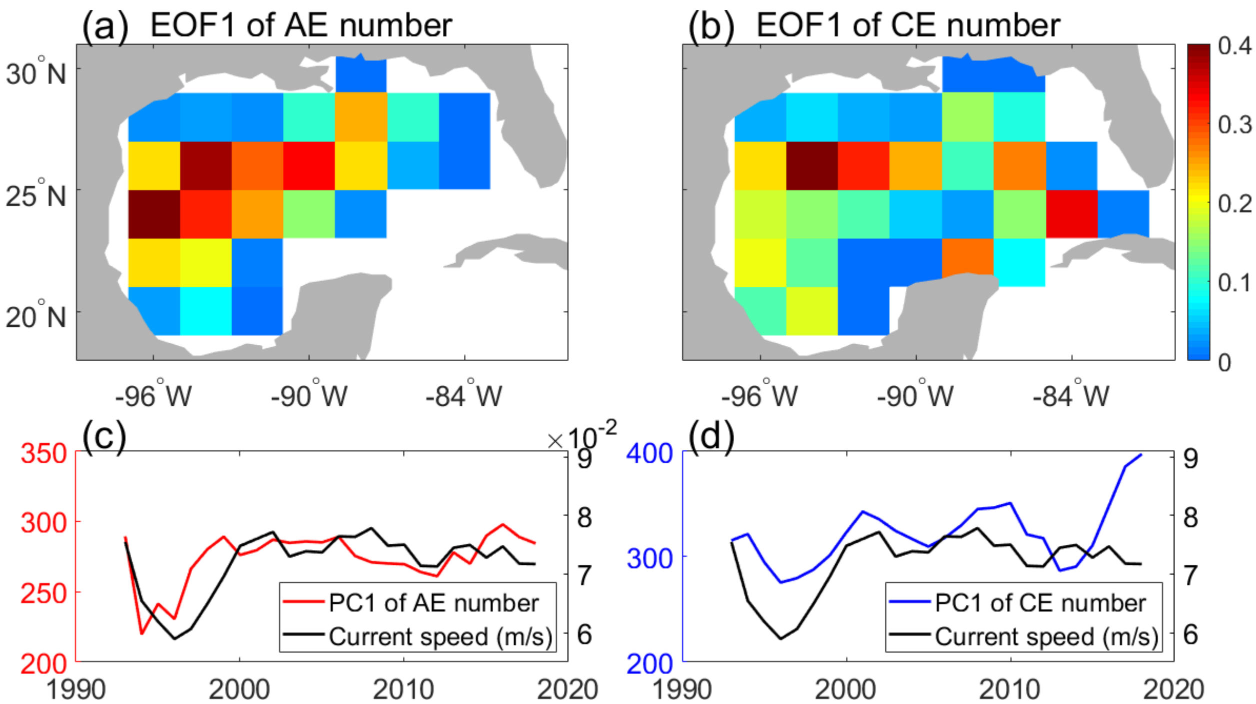

Figure 12. (a) Mode-1 EOFs of annual AE number. (b) Mode-1 EOFs of annual CE number. (c) Mode-1 PC of annual AE number. (d) Mode-1 PC of annual CE number. The black line in (c, d) represents the surface current speed averaged in the western GoM. Note that the mode-1 PCs of AE and CE number and the surface current speed were smoothed with a 5-point moving average.

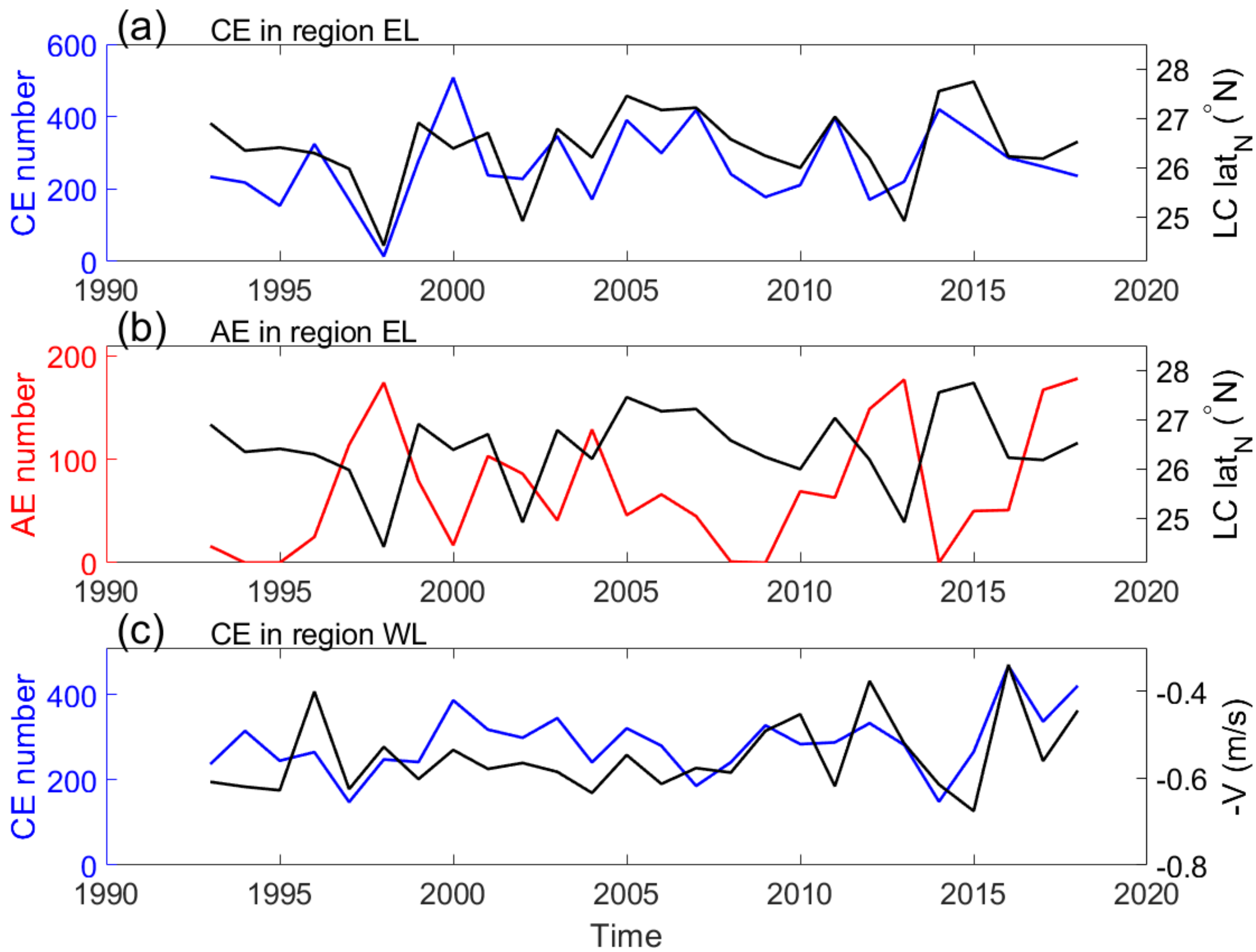

Figure 13. (a-b) Annual CE number (blue) and AE number (red) in the eastern part of the LC (region EL). (c) Annual CE number (blue) in the western part of the LC (region WL). The black line in (a, b) represents the annual mean of the northern position of the LC and the black line in (c) represents the annual mean of the minus surface current speed averaged in the region marked by the magenta square in Figure 5d. The Eastern part (region EL) and the western part (region WL) of the LC are marked in Figure 5c.

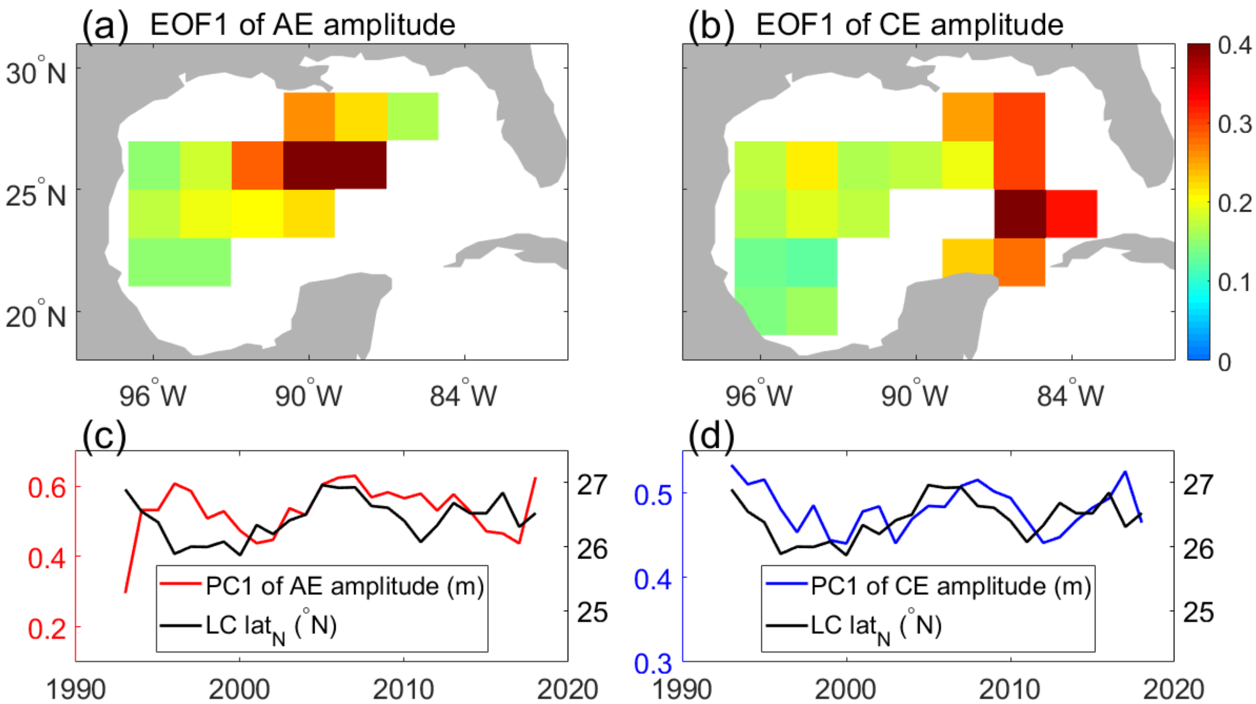

Figure 14. (a) Mode-1 EOFs of the annual median amplitude of AEs. (b) Mode-1 EOFs of the annual median amplitude of CEs. (c) Mode-1 PCs of the annual median amplitude of AEs. (d) PCs of the annual median of CEs. The black line in (c, d) represents the northern position of the LC. Note that the mode-1 PC time series were smoothed with a 5-point average.